Journal of Materials Chemistry C

Accepted Manuscript

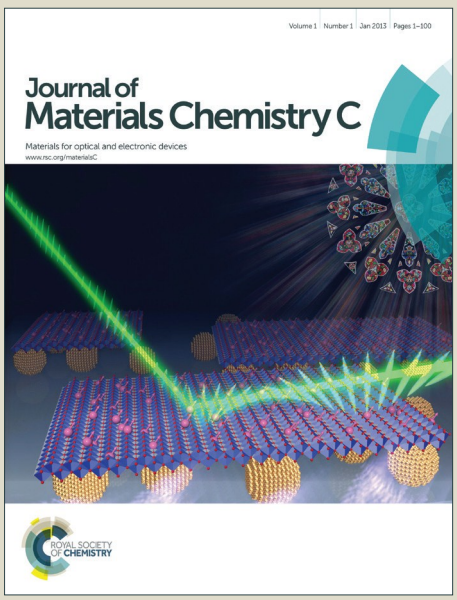

ROYAL SOCIETY OF CHEMISTRY

www.rsc.org/materialsC

Journal of Materials Chemistry C

ARTICLE

Novel monomeric and dimeric pyrene comprising supramolecular AIEE active nano-probes utilized in selective "off-on" trivalent metal and highly acidic pH sensing with live cell applications

Received 00th January 20xx,
Accepted 00th January 20xx

DOI: 10.1039/x0xx00000x

www.rsc.org/

Muthaiah Shellaiah,[a] Turibius Simon,[b] Venkatesan Srinivasadesikan,[c] Chein-Ming Lin,[b] Kien Wen Sun,[a,d*] Fu-Hsiang Ko,[b] Ming-Chang Lin[c] and Hong-Cheu Lin[b]

Two novel pyrene containing monomeric and dimeric schiff base derivatives **PCS1** and **PCS2** has been synthesized *via* one-pot reaction and their Nano-*J*- type aggregation with induced emission enhancements (AIEE) were well demonstrated by UV-Vis/PL, Transmission Electron Microscope (TEM), Dynamic Light Scattering (DLS), time resolve photoluminescence (TRPL), and live cells imaging studies. Contrast to **PCS2**, **PCS1** in CH_3CN exhibits the fluorescence "OFF-ON" sensor selectivity to transition trivalent metal ions (Fe^{3+}, Cr^{3+} and Al^{3+}) among other metals, *via* PET inhibition with excimer **PCS1**-**PCS1*** formation. The 2:1 stoichiometry of sensor complexes **PCS1**---M^{3+} (M = Fe/ Cr/ Al) were calculated from job plots based on their PL titrations. In addition, the binding sites of sensor complexes **PCS1**---M^{3+} were well recognised from the ^{1}H NMR titrations and supported by ESI (+Ve) mass and FTIR analysis. Additionally, fluorescence reversibilities of **PCS1**---M^{3+} were observed via consequent additions of M^{3+} ions and PMDTA, respectively. Further, the detection limits (LODs) and the association constants (K_as) values of **PCS1**---M^{3+} complexes were calculated by standard deviation and linear fittings. Likewise, the quantum yield (Φ), TEM analysis, pH effect, density functional theory (DFT) studies and time resolve photoluminescence (TRPL) studies were investigated for the **PCS1**---M^{3+} sensor complexes. More importantly, confocal fluorescence microscopy imaging in Raw264.7 cells showed that **PCS1** could be used as an effective fluorescent probe for detecting transition trivalent metal ions (Fe^{3+}, Cr^{3+}, and Al^{3+}) in living cells. Impressively, both **PCS1** and **PCS2** evidenced the "OFF-ON" sensing to highly acidic pHs (1-3) with live cell applications.

Introduction

Supramolecular chemistry has long been utilized to create nano-architectures with fascinating molecules with varieties of promised applications.[1-3] The major supramolecular morphologies are derived from non-covalent interactions such as hydrogen bonds, Vander Waals forces, π-π stacking, and dipole–dipole interactions.[4] Among these, π-π stacking interactions are found to be widely used for the construction of *J* or *H*-type three-dimensional supramolecular designs in both chemical and biological systems.[5,6] Recently, AIEE probes have been reported with *J* or *H*-type nano-aggregation for the detection of many diseases and also for several analyte detections with living cell applications.[7-9] But, synthetic difficulties were observed in the design of those selective probes.[10-12] Therefore, to avoid such synthetic issues, few schiff base probes have been reported with effective AIEE properties.[13-15] Akin to AIEE studies, chemical, biological, anions, amino acids, pH and metal ion sensors are also considered as the exciting research filed.[16-18] In these deliberations, many reports are available towards various analytes including emphasized transition metal ions and for wide range of pHs.[19-21]

Attributed to the biological and environmental importance of Fe^{3+}, Cr^{3+}, and Al^{3+} ions, many sensory probes have been reported.[22-24] In between Fe^{3+}, Cr^{3+}, and Al^{3+} ions, variety of cell functions such as muscle and brain function, haemoglobin formation, and electron transport in DNA and RNA synthesis were carried out vitally by Fe^{3+} ions.[25] However, by enhancing the production of reactive oxygen species (ROS), excess amounts of Fe^{3+} may cause damage to nucleic acids and proteins in a living cell.[26] On the other hand, Cr^{3+} ions also plays an important role in the maintenance of an effective carbohydrates, lipid and protein metabolism.[27] But, its deficiencies causes sugar metabolic disorder resulting in

[a] Department of Applied Chemistry, National Chiao Tung University, Hsinchu 300, Taiwan. * E-mail: kwsun@mail.nctu.edu.tw
[b] Department of Materials Science and Engineering, National Chiao Tung University, Hsinchu 300, Taiwan.
[c] Center for Interdisciplinary Molecular Science, Department of Applied Chemistry, National Chiao Tung University, Hsinchu 300, Taiwan.
[d] Department of Electronics Engineering, National Chiao Tung University, Hsinchu 300, Taiwan.

Electronic Supplementary Information (ESI) available: [^{1}H, ^{13}C-NMR, ESI-mass, TEM and TRPL data of compounds and sensor properties]. See DOI: 10.1039/x0xx00000x

engendering diabetes and cardiovascular disease risk, even cataract, blindness, uremia, and so on.[28] Similarly, excessive intake of Cr^{3+} ions also leads to genotoxic effects as well.[29] Conversely, human illnesses such as dementia and encephalopathy, Parkinson and Alzheimer diseases are believed to be attributed to the toxicity of Al^{3+}.[30, 31] Long-sighted the importance of these trivalent transition metal ions, several methods has been reported for their detection including plasma-mass spectroscopy, inductively coupled plasma-atomic emission spectrometry, inductively coupled atomic absorption/emission spectroscopy, and voltammetry.[32-34] However, most of them are low in selectivity and sensitivity with need of expensive instruments. In contrast, simple and cost effective fluorescent "off-on" sensor selective probe for trivalent cations are found to be impressive with wide applications in medicine, biology, and environmental chemistry.[35-37] Similar to transition trivalent sensors, developing sensory probes for low acidic pHs 1-3 is also found to be essential for many applications, such as nuclear fuel reprocessing, the separation of rare-earth metals, and the recycling and reuse of strong acids in industrial processes.[38, 39]

Based on internal charge transfer (ICT), photoinduced electron transfer (PET), chelation-enhanced fluorescence (CHEF), excimer/exciplex formation, and fluorescence resonance energy transfer (FRET) mechanisms, various selective "off-on" fluorescent sensors for M^{3+} (M=Fe/Cr/Al) ions were reported.[40, 41] Among them, due to its simplicity with applications in many opto-electronic and biological systems, PET and excimer/exciplex formation mechanisms are highly impressive.[42, 43] In this concern, pyrene containing probes are very motivating because of their faster response *via* PET and excimer/exciplex formation towards specific species of interest.[44-46] On the other hand, many pyrene containing moieties evidenced the "off-on" fluorescence sensor responses towards variety of analytes and also forms *J* or *H*-type aggregation in its AIEE properties with many biological and environmental applications.[47-49] Excitingly, pyrene containing schiff base based sensor and AIEE probes are also available with lesser synthetic steps and specific selectivity towards variety of analytes.[50, 51] Hence, by considering the importance of both AIEE and sensor selectivity properties, we tend to develop such pyrene containing monomeric and dimeric schiff base derivatives with AIEE characteristics and utilized as "off-on" fluorescent sensor to M^{3+} (M = Fe/ Cr/ Al) ions.

Herein, we have successfully synthesized novel pyrene containing monomeric and dimeric schiff base derivatives **PCS1** (in CH_3CN) and **PCS2** (in DMSO) *via* one-pot reaction and their AIEE active *J*-type nano-aggregation with H_2O (0-90%) was well established by UV/PL, TEM, DLS, TRPL and live cell imaging studies. Contrary to **PCS2**, the better "off-on" fluorescent sensor selectivity of **PCS1** (in CH_3CN) to M^{3+} (M = Fe/ Cr/ Al) ions were demonstrated by UV/PL, ^1H NMR, ESI (+Ve), and density functional calculations studies with live cell applications. Further, highly acidic pH (1-3) "off-on" fluorescent sensor responses were proved by live imaging studies.

Experimental Studies

Materials and methods

All anhydrous reactions were carried out by standard procedures under nitrogen atmosphere to avoid moisture. The solvents were dried by distillation over appropriate drying agents and reactions were monitored by TLC plates. ^1H and ^{13}C NMR were recorded on a 300 MHz Bruker spectrometer. The chemical shifts (δ) are reported in ppm and coupling constants (*J*) in Hz and relative to TMS (0.00) for ^1H and ^{13}C NMR, (s, d, t, q, m, and dd means single, double, ternary, quadruple, multiple, and doublet of doublet, respectively), and d-chloroform [at 7.26 ppm (^1H NMR) & 77.0 ppm (^{13}C NMR)] and d_6-DMSO [at 2.49 (^1H NMR) and 39.52 ppm (^{13}C NMR)] were used as references. Mass spectrum [ESI(+Ve)] was obtained from the respective mass spectrometer. Absorption and fluorescence spectra were measured on HITACHI, U-3310 Spectrophotometer and HITACHI F-7000 Fluorescence Spectrophotometer, respectively. Identification and purity of the compound **PCS1** was characterized by NMR (^1H & ^{13}C) and ESI (+Ve)-Mass. Time-resolved photoluminescence (TRPL) spectra were measured using a home-built single photon counting system. Excitation was performed using a 410 and 420 nm diode laser (Picoquant PDL-200, 50 ps fwhm, 2 MHz). The signals collected at the excitonic emissions of solutions were connected to a time-correlated single photon counting card (TCSPC, Picoquant Timeharp 200). The emission decay data were analyzed with the biexponential kinetics in which two decay components were derived. The lifetime values (τ_1 and τ_2) and pre-exponential factors (A_1 and A_2) were determined and summarized. 0-14 pH buffers were freshly prepared as per the literature.[52] TEM studies were done by JEOL-JEM-2100. The size distribution of **PCS1** in CH_3CN (at 0 and 80% H_2O) and **PCS2** in DMSO (at 0 and 80% H_2O) were also characterized by dynamic light scattering BECKMAN COULTER Delsa^{TM} Nano C particle analyzer. Fourier transform Infrared spectroscopy (FTIR) were analysed by Perkin Elmer - 100 FT-IR SPECTRUM ONE spectrometer. The powder XRD data of bare AuNPs was obtained from BRUKER AXS D2 Phaser (a26-x1-A2BOE2B). Fluorescence microscopic images were taken using Multiphoton and Confocal Microscope System, Leica, Germany, TCS-SP5-X AOBS.

Sensor titrations

Compound **PCS1** was dissolved in CH_3CN and Na^+, Ni^{2+}, Fe^{3+}, Cd^{2+}, Cr^{3+}, K^+, Cu^{2+}, Fe^{2+} and Al^{3+} metal cations were dissolved in water medium at $1x10^{-3}$ M concentration from their respective chloro and perchlorate compounds. Similarly, Ag^+, Co^{2+}, Zn^{2+}, Pb^{2+}, Mn^{2+}, and Hg^{2+} metal cations were dissolved in water medium at $1x10^{-3}$ M concentration from their respective acetate salts. Penta methyl

diethylene diamine (PMDTA at $1x10^{-3}$ M) was dissolved in CH_3CN for sensor reversibility.

FTIR analysis

For FTIR analysis the metal (M^{3+} = Fe^{3+} / Cr^{3+} / Al^{3+}) ions in H_2O concentrations were fixed at 1 equiv. and **PCS1** concentrations were varied as 1 and 2.0 equivs., in CH_3CN. The complexes were stirred at 45˚C for 12 hrs, dried in oven at 100 ˚C for 3 hrs. Then grinded with KBr to make pellets for the measurements.

Procedure[53-57] for the synthesis of compound PCS1 and PCS2

PCS1: (a) To 1 equiv. of 2-aminoethanethiol (commercially known as cysteamine) in 50 ml of methanol, 1 equiv. of Pyrene-1-carboxaldehyde was added with constant stirring under nitrogen and then refluxed for 12 hrs. The reaction was monitored by TLC, after completion, the reaction mixture was cooled and the solvent was evaporated to give the crude product, which was recrystallized from ethanol to afford pure compound as pale yellow solid.

(c) 250 mg of **PCS2** was dissolved in 1 ml of DMSO, then diluted with dichloromethane to 25 ml. To the above mixture, 2 ml of 1 M HCl solution was added and vigorously stirred for 3 hours at 40˚C. Then cool to room temperature, poured in to water and extracted with 50 ml CH_2Cl_2. The crude product **PCS1** was obtained after distillation of organic solvent, recrystallized from ethanol provide the pure **PCS1** with 72% yield. The formation of **PCS1** from **PCS2** was well confirmed by ESI (+Ve) mass spectrum in solution state (**PCS2** in 1M HCl).

2-((pyren-1-ylmethylene)amino)ethanethiol (**PCS1**): pale yellow solid; 88% / 72% yields; ^{1}H NMR (300 MHz, $CDCl_3$) δ: 1.63 (s; 1H (-SH)), 3.31 (t, *J* = 6.6 Hz, 2H (-CH_2)), 4.18 (t; *J* = 6.6 Hz, 2H (-CH_2)), 8.94 – 8.15 (m, 7H), 8.44 (d, *J* = 7.8 Hz, 1H), 8.75 (d, *J* = 8.7 Hz, 1H), 9.26 (s, 1H (-CH=N)); ^{13}C NMR (75 MHz, $CDCl_3$) δ: 40.08, 61.11, 122.41, 124.47, 124.69, 124.82, 125.57, 125.78, 125.98, 126.24, 127.31, 128.23, 128.49, 128.61, 129.80, 130.44, 131.12, 132.84, 161.50; ESI (+Ve) mass: calculated: m/z = 289.3 (M^+, 100%); Found: (a) m/z = 289.3 [(M^+)100%]; (c) m/z = 288.2 [(M-1)$^+$, 100%].

PCS2: (b) To 1 equiv. of 2,2'-disulfanediyldiethanamine[58] (commercially known as cystamine; obtained from cystamine dihydrochloride) in 50 ml of methanol, 2 equivs., of Pyrene-1-carboxaldehyde was added with constant stirring under nitrogen and then refluxed for 18 hrs. The reaction was monitored by TLC, after completion, the reaction mixture was cooled and the solvent was evaporated to give the crude product, which was recrystallized (three times) from ethanol to afford pure compound as light brown solid.

(c) 250 mg of **PCS1** was dissolved in 25 ml of dichloromethane. To that mixture, 2 ml of 1 M NaOH solution was added and vigorously stirred for 3 hours at 40˚C. Then cool to room temperature, poured in to water and extracted with 50 ml CH_2Cl_2. The crude product **PCS2** was obtained after distillation of organic solvent, recrystallized (three times) from ethanol provide the pure **PCS1** with 82% yield. The formation of **PCS2** from **PCS1** was well established by ESI (+Ve) mass spectrum in solution state (**PCS2** in 1M NaOH).

2,2'-disulfanediylbis(N-(pyren-1-ylmethylene)ethanamine) (**PCS2**): Light brown solid; 76% / 82%; ^{1}H NMR (300 MHz, d_6-DMSO) δ: 3.26 (t; *J* = 6.4 Hz, 4H (-CH_2)), 4.13 (t; *J* = 6.4 Hz, 4H (-CH_2)), 8.04 – 8.32 (m, 14H), 8.47 (d, *J* = 8.1 Hz, 2H), 9.01 (d, *J* = 9.6 Hz, 2H), 9.39 (s, 2H (-CH=N)); ^{13}C NMR (75 MHz d_6-DMSO) δ: 31.15, 61.81, 123.02, 123.30, 123.90, 124.11, 124.39, 124.47, 125.12, 125.30, 125.51, 126.00, 126.10, 126.42, 126.58, 126.79, 126.84, 127.27, 127.64, 127.72, 127.90, 128.18, 128.65, 128.98, 129.66, 130.44, 130.81, 131.14, 131.27, 132.70, 136.47, 131.17, 161.84; ESI mass: calculated: m/z = 577.3 (M^+, 100%); Found: (a) m/z = 577.3 [(M^+)100%]; (c) m/z = 577.3 [M^+, 100%].

Procedure for fluorescence imaging

AIEE:

Raw264.7 cells were cultured in DMEM (Dulbecco's Modified Eagle's Medium, high glucose) supplemented with 10% FBS at 37°C and 5% CO_2. Cells were plated on 14 mm glass coverslips and allowed to adhere for 24 hours.

The cell image was performed in PBS with 10 μM **PCS1** or **PCS2** dissolved in DMSO. The cells cultured in DMEM were treated with of 10 μM **PCS1** or **PCS2** dissolved in DMSO-sterilized PBS (pH7.4) and incubate for 30 min and 12 hours at 37°C. The culture medium was removed, and the treated cells were washed with PBS (2 ml) before observation. Fluorescence imaging was performed with a Multiphoton and Confocal Microscope System, Leica, Germany, TCS-SP5-X AOBS. The cells were excited with a white light laser at λ_{ex} = 355 nm at 6% output and collecting emission between 430 ± 480 nm

PCS1---M^{3+}:

PCS1 was also applied to living cell imaging. For the detection of M^{3+} (M = Fe/ Cr/ Al) in living cells. The RAW264.7 cells The cells cultured in DMEM were treated with of 20 μM M^{3+} dissolved in sterilized PBS (pH7.4) and incubate for 30 min at 37°C and then wash the treated cells for three times with 2 ml PBS to remove the remaining metal ions. Add 2 ml of culture media to the cell culture and treat the cell culture with 20 μM of **PCS1** dissolved in DMSO followed by incubate (60 min at 37°C). The culture medium was removed, and the treated cells were washed with PBS (2 ml) before observation. Fluorescence imaging was performed through a confocal microscope system mentioned previously. The cells were excited with a white light laser at λ_{ex} = 410 nm at 6% output and collecting emission between 480 ± 525 nm (**PCS1**---M^{3+}).

PCS1 and **PCS2** at pH = 3:

The cell image was performed in pH = 3 buffer with 10 μM **PCS1** or **PCS2** dissolved in DMSO. RAW264.7 cells cultured in DMEM were

treated with of 10 μM **PCS1** or **PCS2** dissolved in DMSO-sterilized pH = 3.0 buffer and incubate for 50 min., at 37°C [Note: Initially, MTT assay (not shown) were performed at pH = 3.0 buffer and found that up to 50 min., the cell viabilities were not affected for both compounds. Hence, fixed the cell imaging time as 50 min., at pH = 3.0]. The culture medium was removed, and the treated cells were washed with PBS (2 ml) before observation. Fluorescence imaging was done by a confocal microscope system mentioned earlier. The cells were excited with a white light laser at λ_{ex} = 410 nm at 6% output and collecting emission between 480 ± 525 nm.

TEM and DLS studies

For TEM analysis, the samples (100 times diluted) were drop-casted on copper grid then allowed to vacuum dry for overnight and the TEM studies of AIEE were done with JEOL-JEM-2100 instrumental set up. Corresponding TEM samples were subjected to DLS analysis with BECKMAN COULTER Delsa ^{TM} Nano C particle analyser.

Results and discussion

Synthesis and AIEE properties of PCS1 and PCS2

As shown in Schemes 1a and b, **PCS1** (monomer) and **PCS2** (dimer) were synthesized *via* one pot condensation of pyrene-1-carboxaldehyde and cysteamine (or) cystamine (**CS1** / **CS2**) in methanol with 88% / 76% yields. Both compounds were characterized by ^{1}H, ^{13}C NMR and Mass [ESI (+Ve)] analysis (Figs. S1-S6, ESI). Similar to Schemes 1a and b, both **PCS1** and **PCS2** were also synthesized *via* Scheme 1c. In which, both of them are act as reactants in presence of 1M NaOH / HCl solution, to provide **PCS2** / **PCS1** with 72% /82% yields, correspondingly. Formation of both compounds from their respective monomer / dimer were demonstrated from similar ^{1}H, ^{13}C NMR spectra (not shown) along with their ESI (+Ve) mass in NaOH / HCl solutions (Figs. S7 and S8, ESI).

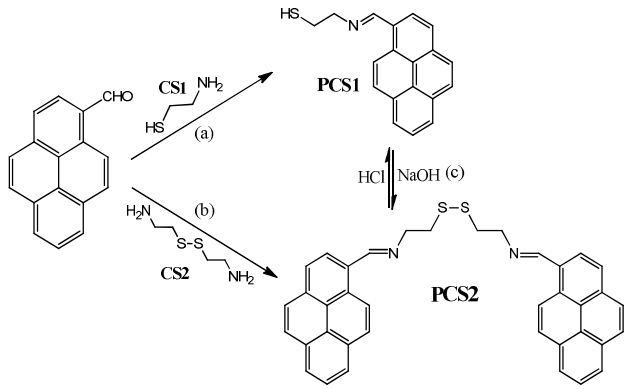

Scheme 1. Synthesis of **PCS1** and **PCS2** (a) MeOH, reflux, 12 hrs, 88%; (b) MeOH, reflux, 18 hrs, 76%; (c) 1M HCl /1M NaOH, CH_2Cl_2, 24 hrs, 72%/82% (**PCS1**/**PCS2**).

The TRPL spectra of **PCS2** (in DMSO) in presence of 1M HCl solution reveals that, the highly acidic condition will rapidly affects its decay life time from 1.345 ns to 0.72 ns as shown in Table 1 and Figure S9 (ESI). The faster and longer decay components (A_1 and A_2) were also affected along with ultra-fast and longer decay constants (τ_1 and τ_2) for **PCS2** + HCl (1M) as summarized in Tables S1. The green emission may arose from the –S-S bond cleavage at high acidic condition to form **PCS1**, which further leads to self-aggregation with excimer formation. Thus, the acidic pH sensing abilities of both monomer and dimer compounds were further examined latter.

The higher electronegative nature of sulphur atom plays the prime role in the formation of **PCS1** and **PCS2** from each other. To prove this hypothetical concept, optimized electro static potentials (Gaussian 09) of **PCS1** and **PCS2** were taken into account. As noticed in Figs. 1a and b, the electro-static potential of both monomer (**PCS1**) and dimer (**PCS2**) are majorly located on sulphur atoms. Hence, upon maintaining the solvent pH from highly acidic or basic condition, the S-S bond cleavage or bond formation might be highly favourable to provide monomer / dimeric compounds. Further, electro-static potential (ESP) of them also reveals the possibility of enhanced crystallinity during dimeric **PCS2** formation. Henceforth, the powder XRD patterns were examined to confirm the improved rigid-crystalline nature of **PCS2**. Figs. 1c and d, revealed the XRD pattern of **PCS1** and **PCS2** as described follows. Contrast to **PCS2**, the **PCS1** demonstrated more number of XRD peaks due to its low crystallinity. Similar XRD patterns were reported by Qu et. al. for pyrene monomer.[59] But, during the oligomerization, those pattern were affected with improved crystallinity. For **PCS1**, the major XRD peaks were observed at (2Theta): 11.39, 14.97, 17.01, 18.54, 22.28, 24.77, 28.82, 32.25, 35.52, 38.94, 42.37, 46.10, 49.69, 53.58, and 57.39 along with some various minor peaks. This might be attributed to its lower crystalline property, driven from the unrestricted possible rotation (or) bending of free thiol unit with attached schiff base moiety. On the other hand, **PCS2** notifies only fewer XRD patterns at (2Theta): 11.38, 15.25, 18.51, 26.69, 35.77, 45.40, 55.03, 65.39, and 76.28. Thus, it is well established that, the formation of disulphide (-S-S-) bond in the dimer will improve the rigidity by restriction of free rotation with attached schiff base. As stated earlier, the electronic clouds in ESP (Figure 1b) are located on –S-S bond might improve the crystallinity / rigidity of **PCS2** *via* inhibited intramolecular rotation. Which also hints that **PCS2** may aggregate faster than that of **PCS1**, as explained next.

Initial evaluation of monomer emission revealed that, the presence of polar protic solvents such as ethanol and water were evidenced the peaks between 365 – 400 nm, in which maxima appeared at 385 and 421 nm for PCS1 as well as at 387 and 425 nm for PCS2. However, the maxima peaks between 365 – 400 nm were disappeared in polar aprotic solvents like CH_3CN and DMSO, this might due to the solvent effect. Since, our compounds were showed the greater solubility in polar aprotic solvents, we have dissolved **PCS1** and **PCS2** in CH_3CN and DMSO, respectively. Whereas, polar protic solvents solidified rapidly during dissolution. During the incremental addition of H_2O into **PCS1** (10 μM; in CH_3CN) and **PCS2** (10 μM; in DMSO), the aggregation induced-

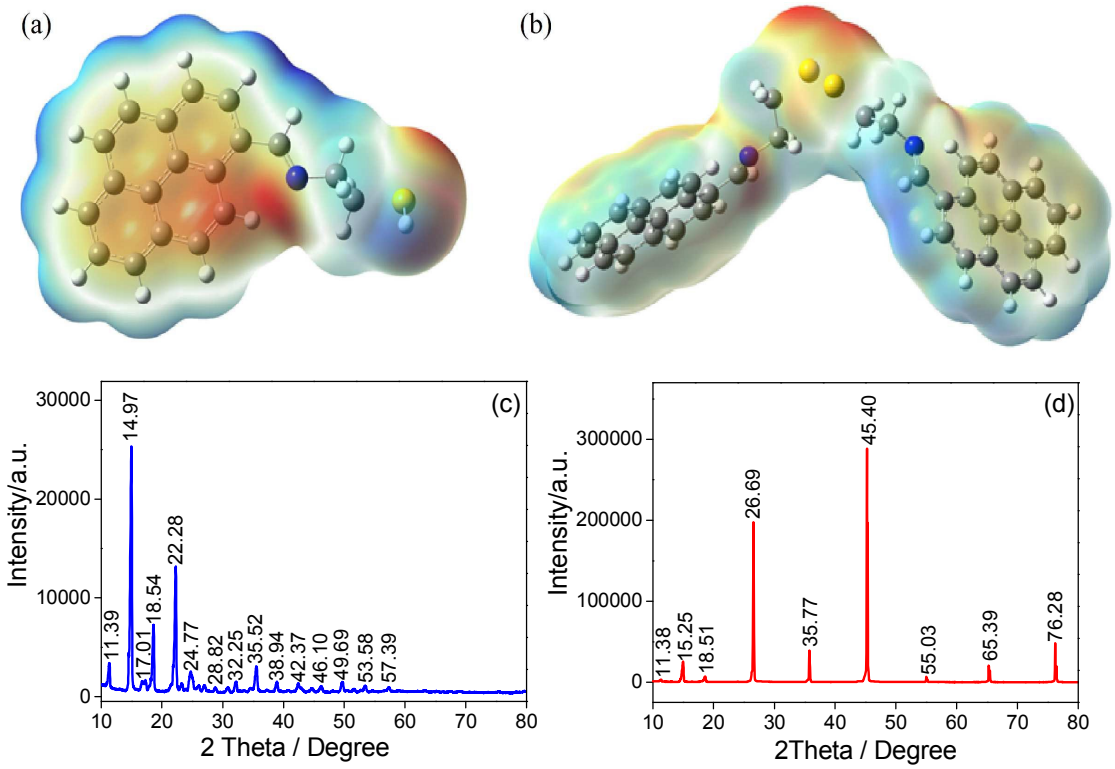

Fig. 1 Optimized electrostatic potential of (a) **PCS1** and (b) **PCS2**; XRD pattern of (c) **PCS1** and (d) **PCS2**.

emission enhancement (AIEE) characteristic of those probes were observed. As revealed by Figs. 2a and c, upon addition of H_2O fraction (f_w) from 0% to 90%, the UV-Vis peaks at 356 / 352 nm (**PCS1** /**PCS2**) were quenched and red shifted to 364 / 357 nm (at 80% / 60% of f_w), with the appearance of newer peaks at 393 and 396 nm, respectively. Correspondingly, the PL peaks at 421 / 425 nm (**PCS1** /**PCS2** at 0% f_w) were also red shifted to 465 / 469 nm (at 80% / 60% of f_w; λ_{ex} = 355 nm), respectively, as shown in Figs. 2b and d. Further, the fluorescent quantum yield (Φ_f) of **PCS1** / **PCS2** were increased rapidly during their AIEE characteristics with f_w (0-90%). As exposed in Fig. 2e and Table 1, the maximum quantum yield values of **PCS1 / PCS2** (Φ_f = 0.011 / 0.0152, at 0% of f_w) were increased (Φ_f = 0.5526 / 0.854, at 80% / 60% of *fw*, correspondingly) to 50 / 56 folds. The photograph envisioned in Fig. 2f, illustrate the aggregation induced emission of **PCS1** and **PCS2** in H_2O (0-90%) by visualizing the strong blue emission under UV-irradiation at 365 nm. In AIEE process, the π-π stacking of pyrene units were influenced by amplified addition of water fraction from 0-90%, which can be witnessed *via* red shifted UV/PL peaks for both monomeric and dimeric compounds (Figs. 2a-d). At 0%, both **PCS1** and **PCS2** were not have any excimer emission. However, upon incremental addition of water, the improved excimer emission were observed with red shifted peaks. The maximum excimer emissions were established at 60 and 80% of water fractions for **PCS1** and **PCS2**, respectively. Due to the presence of monomers along with excimers, until attained the maximum excimer emissions, their peaks are the combination of both species. Thereafter, as shown in Figs. 2b and d, the peaks were quenched at 90% (**PCS1**) and 70 – 90% (**PCS2**), because of the solvent effect. In which, those concentrations may have only excimer emissions. Furthermore, the higher crystallinity of **PCS2** also support its faster AIEE at 60% of water fraction. However, all the above observations were established merely after 12 hours. Therefore, we analysed the quantum yield (Φ_f) changes with respect to time (0-12 hours, with an equal span of 2 hours) as exposed in Fig. S10 (ESI). From 0-80% / 0-60% (**PCS1** / **PCS2**) of water fractions, the improved AIEEs were witnessed along with increased Φ_f values up to 12 hours. Afterwards, we have not found any more increase in their Φ_f values, hence the time effects were not taken into account further. The red shifted UV-Vis/PL peaks for AIEE properties of **PCS1** / **PCS2** with *fw* (0-90%), illustrated the *J*- type aggregation as reported by Wurthner et. al.[60] During AIEEs, the former UV-Vis peaks of **PCS1** / **PCS2** were observed at 356 / 352 nm and red shifted to 364 / 357 nm (8 / 5 nm shifts) for 80% / 60% of f_w, respectively. Similarly, the initial PL peaks of both were existed at 421 / 425 nm and red shifted to 465 / 469 nm (44 nm shifts) for 80% / 60% of f_w, respectively. Hence, possible *J*-type aggregation was proposed for AIEEs of **PCS1** / **PCS2** as shown in Fig. 3.

The AIEEs of monomer / dimer compounds, were explained hypothetically as follows. Initially, both **PCS1** / **PCS2** (in CH_3CN / DMSO) have PET via lone pair of electron transfers from schiff base nitrogen (-CH=N) to pyrene units or may possess the twisted intramolecular charge transfer (TICT) at 0% of f_w to show their non-emissive property. However, during the incremental addition of

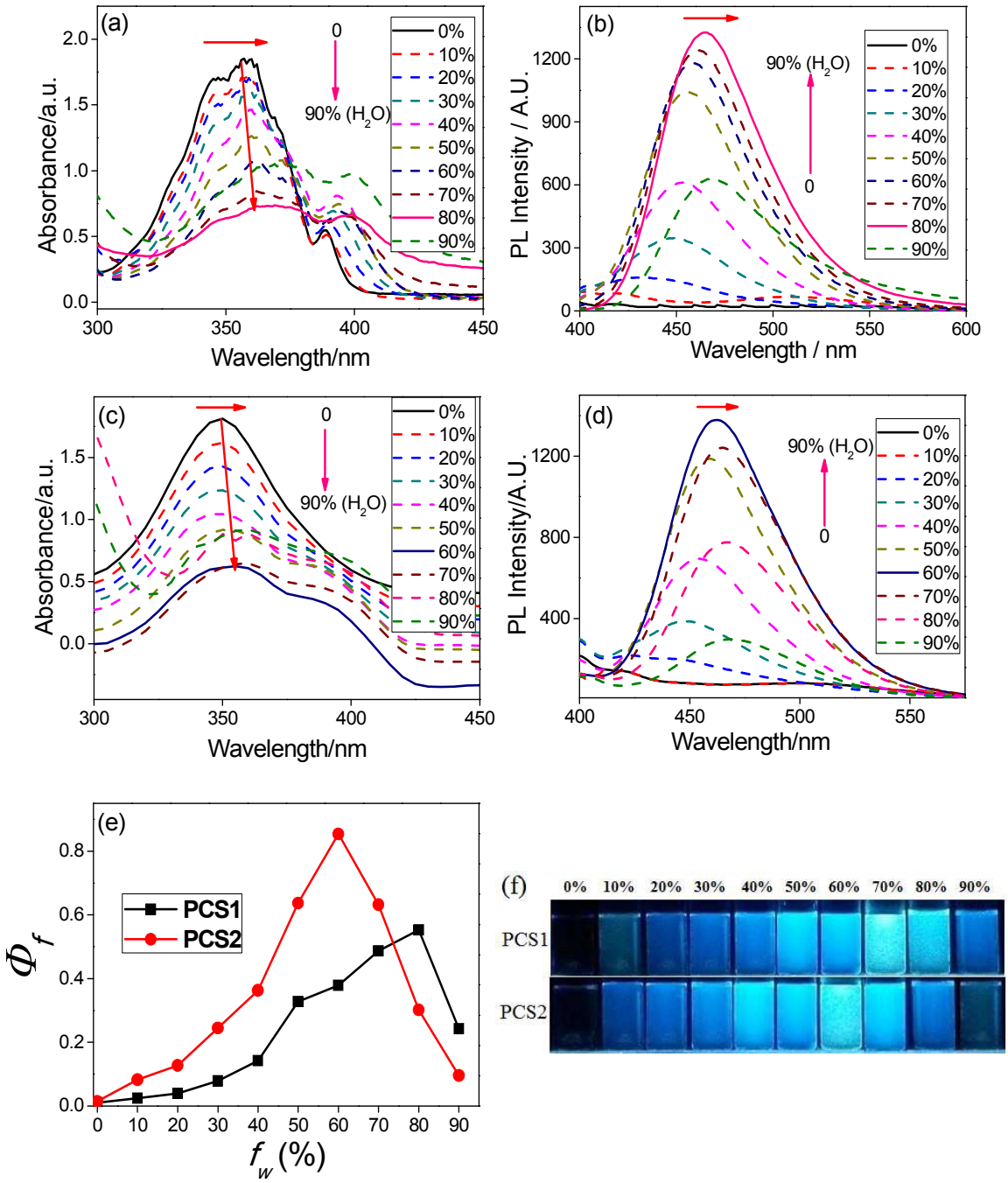

Fig. 2 (a, c) UV-Vis and (b, d) PL spectra of **PCS1** (10 μM in CH_3CN) and **PCS2** (10 μM in DMSO) as a function of increasing water fraction (0-90%; λ_{ex} = 355nm for **PCS1** / **PCS2**); (e) Quantum yield (Φ_f) changes of **PCS1** and **PCS2** with respect to water fraction (f_w in %); (f) Photograph of aggregation induced emission of **PCS1** and **PCS2** visualized under UV-irradiation (λ = 365 nm) (Note: All the above data for AIEE were taken after 12 hours).

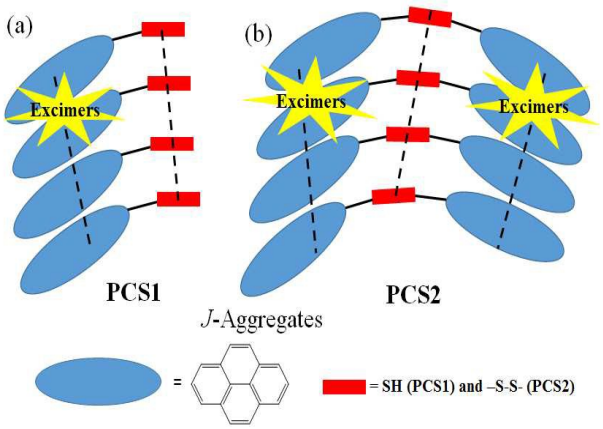

Fig. 3 Schematic illustration of *J*-aggregation of AIEE active **PCS1** and **PCS2**.

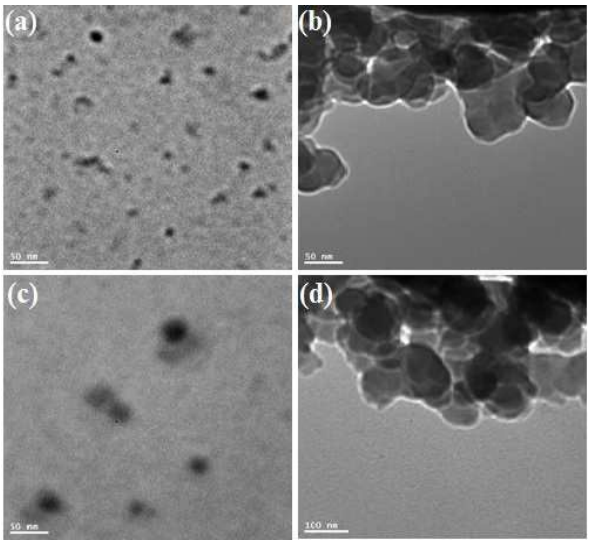

Fig. 4 (a, b) TEM images of **PCS1** in CH_3CN with 0% and 80% of water fraction; (c, d) **PCS2** in DMSO with 0% and 60% of water fraction (Note: TEM images were taken after 100 times dilution).

H_2O to **PCS1** / **PCS2** (in CH_3CN / DMSO), the inhibition of PET / TICT may happened to stimulate their AIEE properties. In contrast to **PCS1**, the crystallinity and bulkiness of **PCS2** leads to faster suppression of PET / TICT and hence shows maximum aggregation at 60% of f_w. The PET mechanisms of **PCS1** / **PCS2** probes were also well demonstrated by Figs. S24, S30-31, and S38 (ESI).

To establish the nano level aggregations of **PCS1** / **PCS2** during their AIEEs studies, TEM and DLS studies were supplemented. The scattered nano-crystals of both monomeric / dimeric schiff bases (in CH_3CN / DMSO) at 0% f_w were visualized in TEM images **(**Figs. 4a and c) at 50 nm scale bar. On the other hand, the aggregation of both **PCS1** / **PCS2** (in CH_3CN / DMSO) at 80% / 60% of f_w were demonstrated by their TEM images (Figs. 4b and d) at 50 and 100 nm scale bars, respectively. Surprisingly, the DLS studies of **PCS1** / **PCS2** (in CH_3CN / DMSO) at 0% f_w revealed that, the nano-crystalline sizes of them as 11.4 ± 1.2 nm and 24.2 ± 4.2 nm, correspondingly (Figs. S11a and S12a). Previously, Wang. et. al. reported the pyrene dimeric units at the range of 2-6 nm.[61] Hence, confirmed that the nano-crystalline sizes are within the acceptable range. Conversely, for **PCS1** / **PCS2** (in CH_3CN / DMSO; at 80% / 60% of f_w), the crystalline sizes were observed at 151.7 ± 19.1 nm and 252.9 ± 63.6 nm, respectively (Figs. S11b and S12b). Notably, the nano-aggregated crystalline sizes of both monomeric / dimeric schiff bases were also proved that, **PCS2** can aggregates rapidly (10 times) at 60% of f_w than **PCS1** (13 times) at 80% of f_w. Therefore, based on TEM and DLS analysis both **PCS1** / **PCS2** and their AIEEs were adjudged as nano-probes and nano-aggregation.

Recently, many AIEE probes were applied in many intracellular applications along with various analytes detection. Henceforth, we protracted our vision towards *in-vitro* cellular applications.[62, 63] As exposed in Fig. 5, When Raw264.7 cells were incubated with **PCS1** / **PCS2** (10 µM in DMSO), no fluorescence was observed at 30 minutes. But, due to the intracellular H_2O induced aggregation, a bright / dismal blue fluorescent images were observed in the Raw264.7 cells after 12 hours. An overlay of fluorescence and bright-field images shows that the fluorescence signals are localized in the intracellular area, indicating a subcellular distribution and good cell-membrane permeability of **PCS1** / **PCS2**. The bright cell image of **PCS1** at 12 hours also verified the greater intracellular penetration of free thiol unit rather than disulphide containing **PCS2**. Moreover, to confirm the bio-compatibility of **PCS1** / **PCS2**, cytotoxicity studies were under taken and both evidenced the 75% cell viability at 20 µM concentration as exposed in Figs. 6a and b.

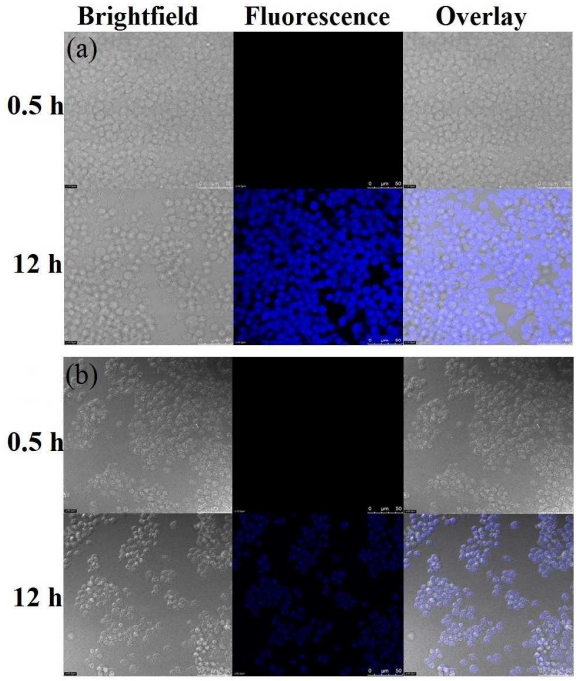

Fig. 5 Fluorescence images of Raw264.7 cells treated with (a) **PCS1** and (b) **PCS2** at 0.5 and 12 hours, respectively. Bright Field image (Left); Fluorescence image (middle); Merged image (right). The scale bar is 50 µM.

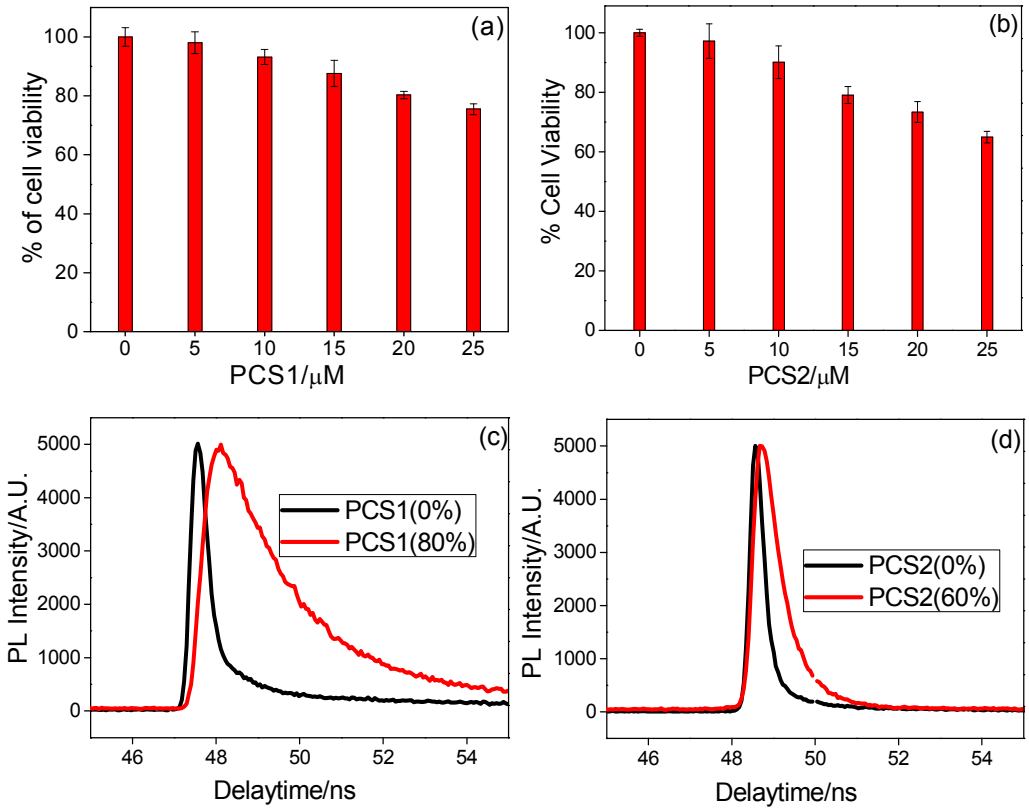

Fig. 6 Cell viability of (a) **PCS1** and (b) **PCS2**; TRPL spectra of (c) **PCS1** in CH_3CN (at 0% and 80% of water fraction; λ_{ex} = 355 nm) and (d) **PCS2** in DMSO (at 0% and 60% of water fraction; λ_{ex} = 355 nm).

Next, TRPL studies were accounted for the AIEEs of **PCS1** / **PCS2** to establish their fluorescent life times. As shown in Figs. 6c and d, the TRPL spectrum of **PCS1** / **PCS2** (in CH_3CN / DMSO; at 0% of f_w) were affected incredibly for **PCS1** / **PCS2** (in CH_3CN / DMSO; at 80% / 60% of f_w). Tables 1 and S1, summarized the respective comparable TRPL changes. Initially, the average TRPL decay constant (τ_{Avg}) values of **PCS1** / **PCS2** (in CH_3CN / DMSO; at 0% of f_w) were found as 3.105 and 1.345 ns, respectively. However, during the AIEE process the decay constant increased to 4.813 and 1.856 ns, for **PCS1** / **PCS2** (in CH_3CN / DMSO) at 80% / 60% of f_w, respectively. Equally, the faster and longer decay components (A_1 and A_2) were also affected along with ultra-fast and longer decay constants (τ_1 and τ_2) for **PCS1** / **PCS2** (in CH_3CN / DMSO) at 80% / 60% of f_w) as summarized in Table S1.

Sensor titrations

Due to the AIEEs of **PCS1** / **PCS2** probes, we checked the possible sensing ability of both in CH_3CN / DMSO and to avoid the controversy between AIEE and sensor selectivity all metal ions concentrations were taken as 1 x 10^{-3} M as described next. Furthermore, on the consideration of "state-of-the-art method", both **PCS1** and **PCS2** can be applied for device based sensory detection of those identified ions in near future. In which, the requirements as follows; (i) should contain the organic semiconducting materials (either p- or n-type) (ii) should not be dissolved in water (iii) should have high thermal stability and (iv) should have selectivity to specific analyte in organic solvents.[64] Since pyrene derivatives have the p-type semiconducting properties, the utilization of **PCS1** and **PCS2** for device based metal ion sensors in organic solvents and their insolubilities in water was considered as advantages. Therefore, while proceeding to sensor titrations, both **PCS1** / **PCS2** (20 μM) in CH_3CN / DMSO (pH 7.0) were investigated towards 20 μM (1 equiv.) of metal ions (Sn^{2+}, Na^{+}, Ni^{2+}, Fe^{3+}, Co^{2+}, Zn^{2+}, Cd^{2+}, Pb^{2+}, Cr^{3+}, K^{+}, Cu^{2+}, Mn^{2+}, Hg^{2+}, Fe^{2+} and Al^{3+}) in H_2O. Surprisingly, contrast to **PCS2**, **PCS1** displayed the selectivity towards Fe^{3+}, Cr^{3+} and Al^{3+} (M^{3+}) metal ions, upon treating with 1 equiv. of metal ions and exhibited the UV-Vis and "OFF-ON" emission peaks at 445 and 515 nm (Figs. 7a and b) , respectively, with red shifts from its origin (**PCS1**; λ_{abs}=356 nm and λ_{em}=421 nm; Φ_f = 0.011). To confirm the specific selectivity, we have evaluated the sensory responses of **PCS1** with many trivalent cations such as Fe^{3+}, Cr^{3+}, Al^{3+}, In^{3+}, Ga^{3+}, Ru^{3+}, Co^{3+}, Mn^{3+} and Ni^{3+}. However, we have evidenced selectivity of **PCS1** to only Fe^{3+}, Cr^{3+} and Al^{3+} ions. Hence, we further proceeded towards detailed analysis of those trivalent sensory properties. The photograph of **PCS1** with different metal ions (envisioned under UV- light irradiations at 365 nm) was well confirmed its selectivity towards

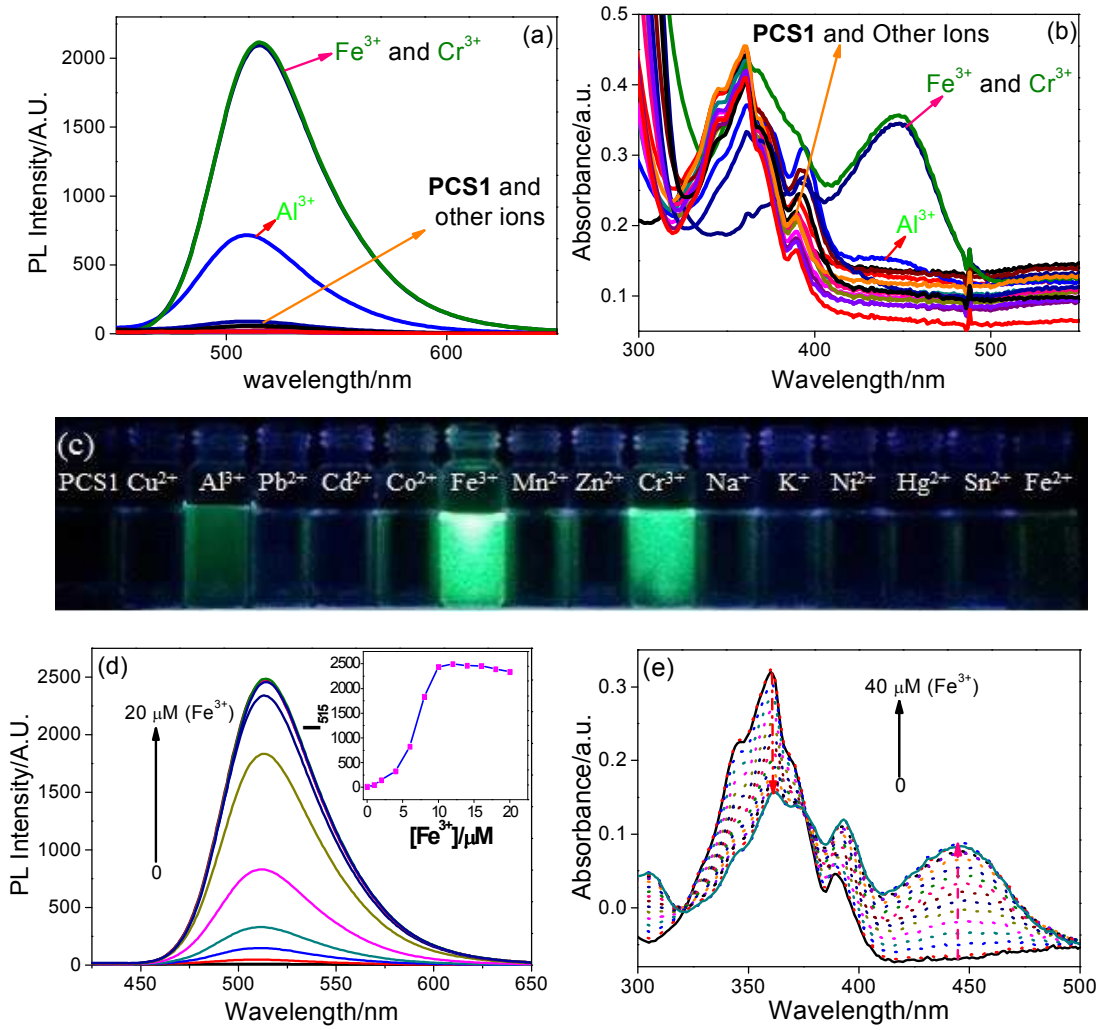

Fig. 7 (a, b) PL and UV-Vis spectra for selectivity of **PCS1** (20 μM in CH_3CN) towards 20 μM (1 equiv.) of metal ions at λ_{ex} = 410 nm; (c) Photograph of sensor selectivity of **PCS1** visualized under UV irradiation (365 nm); (d) PL (λ_{ex} = 410 nm) and (e) UV-Vis sensor titrations of **PCS1** (20 μM in CH_3CN) with 0-20 μM of Fe^{3+} ions in H_2O; PL Inset: Intensity changes as a function of Fe^{3+} concentration.

M^{3+} (M = Fe/ Cr/ Al) ions via strong green emission, as depicted in Fig. 7c. As noted in Figs. 7d and e, by increasing the concentrations of Fe^{3+} [0-20 μM / 0-40 μM (PL / UV) with an equal span of 2 μM in H_2O] the sensitivity of **PCS1** (20 μM in CH_3CN; pH 7.0) towards Fe^{3+} ions were clearly observed. The fluorescence spectrum (Fig. 7d) of **PCS1** (λ_{em} = 421 nm) showed red shifted with turn-on responses rapidly at 515 nm (λ_{ex} = 410 nm) for **PCS1**---Fe^{3+} and the inset illustrated the fluorescence intensity changes as a function of Fe^{3+} concentration. Astoundingly, the histograms (Fig. 8a) of **PCS1**---Fe^{3+}, **PCS1**---Cr^{3+} and **PCS1**---Al^{3+} were found to be 177, 175, and 58 folds, respectively. Similarly, as noted in Table 1, the fluorescent quantum yield (Φ_f) values of **PCS1**---Fe^{3+}, **PCS1**---Cr^{3+} and **PCS1**---Al^{3+} were calculated as 0.601, 0.594 and 0.207 with 55, 54, and 19 folds of enhancements, respectively.

In addition, the above selectivity was further confirmed by dual metal studies as follows. In order to establish the specific selectivity of **PCS1** to M^{3+} ions, we performed the dual metal competitive analysis as noticed in Fig. S13 (ESI). In single metal system (Fig. 8a), all the metal (Sn^{2+}, Na^{+}, Ni^{2+}, Fe^{3+}, Co^{2+}, Zn^{2+}, Cd^{2+}, Pb^{2+}, Cr^{3+}, K^{+}, Cu^{2+}, Mn^{2+}, Hg^{2+}, Fe^{2+} and Al^{3+}) ions concentrations were kept as 20 μM towards **PCS1**. However, for dual-metal (Fig. S13, ESI) studies, two equal amounts of aqueous solutions of M^{3+} (M = Fe/ Cr/ Al) ions with other metal ions (20 μM + 20 μM) were combined and for M^{3+} ions, 40 μM of M^{3+} ions were considered for their effects. From single metal analysis, it is well noted that **PCS1** evidenced the better selectivity to Fe^{3+} and Cr^{3+}, contrary to Al^{3+} ions. Further, in dual metal analysis, obtained results demonstrated the unambiguous selectivity of **PCS1** towards Fe^{3+} and Cr^{3+} ions as noticed in Figs. S13 a-c (ESI). Due to the quenching effect of other metal ions, **PCS1**---Fe^{3+} and **PCS1**---Cr^{3+} sensor systems were found to be quenched little during dual metal analysis. Figs. S13a and b (ESI), shows the effect of other metal ions on **PCS1**---Fe^{3+} and **PCS1**---Cr^{3+} sensors, in which 100 to 150 folds of fluorescence enhancements were still observed. On the other hand, for **PCS1**---Al^{3+} sensor system was

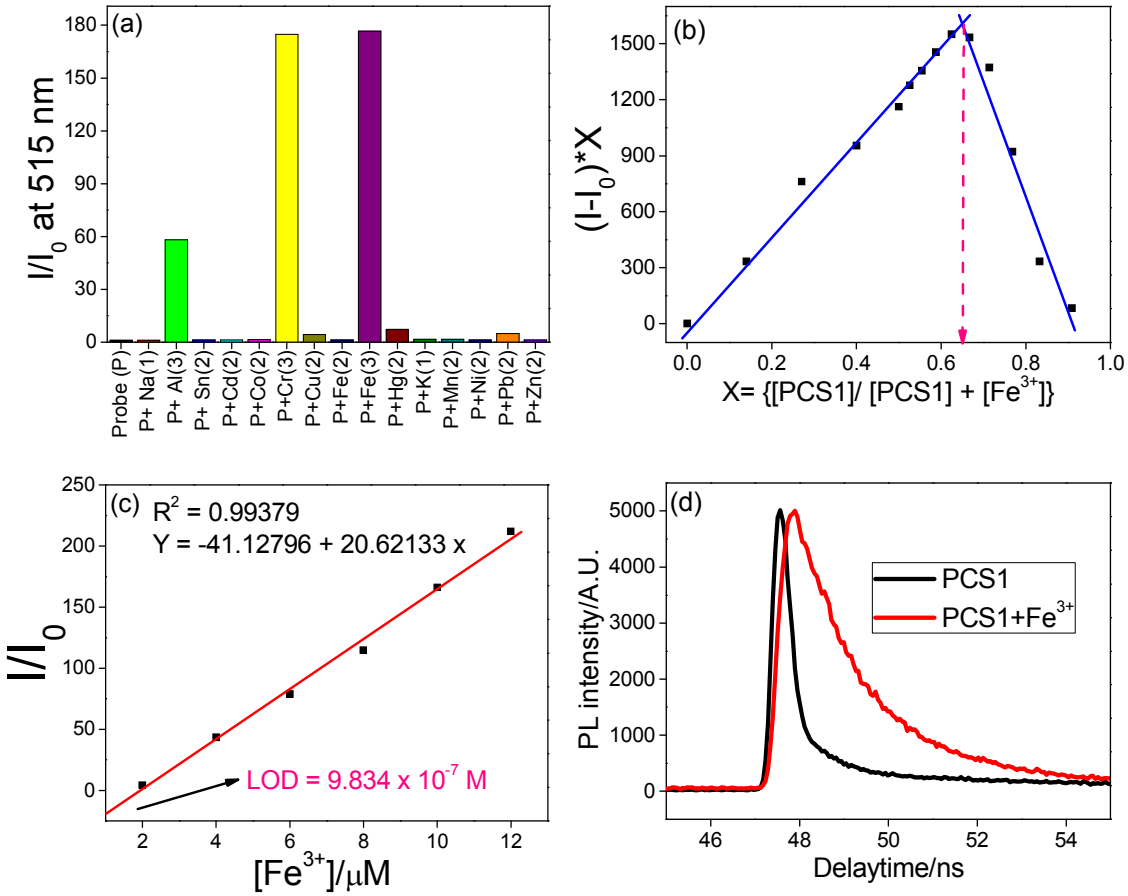

Fig. 8 (a) Histogram representing selectivity of **PCS1** (20 μM in CH_3CN) towards 20 μM (1 equiv.) of metal ions; (b) Job's plot (based on PL intensity changes) between X *vs* $(I-I_0)^*X$, representing 2:1 (**PCS1**---Fe^{3+}; X = 0.656) complex; (c) Linear fitting plot for the detection limit calculation of Fe^{3+} ions; (d) TRPL spectra of **PCS1** and **PCS1**---Fe^{3+}.

completely affected (quenched) by the interference of other metal ions as exposed in Fig. S13c (ESI). Hence, the better selective sensing of **PCS1** to Fe^{3+} and Cr^{3+} ions were confirmed with discrimination of Al^{3+} ions. The specific sensory selectivity of **PCS1** towards M^{3+} (M = Fe/ Cr/ Al) were due to the atom selective coordination of –SH and –CH=N. In which, they have showed the higher affinity to Fe^{3+}, Cr^{3+} and Al^{3+} ions rather than other trivalent cations. On the other hand, specific atomic adaptation may happened during the excimer (**PCS1**-**PCS1**)* formation. In addition, the ionic radii of those ions may also plays the vital role for sensor selectivity. The above statement was well verified by dual metal analysis, which discriminated the Al^{3+} ions in presence of other ions. Hypothetically, the outer most vacant d-orbitals of Fe^{3+} and Cr^{3+} ions ([Ar] $4s^0$ $3d^3$ and [Ar] $4s^0$ $3d^5$) may participated in their better sensitivities than that of Al^{3+} ions ([Ne] or $1s^2$ $2s^2$ $2p^6$). Further, to find out the stoichiometry, detection limits (LODs) and association constants (K_as) of **PCS1**---M^{3+} sensor complexes, individual titrations of **PCS1** with Fe^{3+}, Cr^{3+} and Al^{3+} were performed.

In which, due to the strong fluorescent emission at 515 nm, the I/I_0 and quantum yield (Φ_f) values of **PCS1**---Fe^{3+} sensor response were increased to 177 and 55 folds, respectively (Fig. 7d). Correspondingly, the former UV peak of **PCS1** (λ_{abs} = 356 nm) was quenched and displayed a red shifted newer peak at 445 nm, while titrating with Fe^{3+} (0-40 μM with an equal span of 2 μM in H_2O) ions as shown in Fig. 7e. Impressively, similar observations were established during the titrations of **PCS1** with Cr^{3+} and Al^{3+} ions as exposed in Figs. S14 and S15 (ESI). Based on the above PL observations, the stoichiometry of **PCS1**---M^{3+} (M = Fe/ Cr/ Al) were calculated through job's plots[65] as noticed in Figs. 8b and S16 (ESI). The stoichiometry of **PCS1**---M^{3+} were established by plotting X *vs* $(I-I_0)^*X$; where X is the mole fraction, I and I_0 are the fluorescent intensities of **PCS1** at 515 nm in presence and absence of respective metal ions concentration. Upon the addition of 0-20 μM of M^{3+} (with an equal span of 2 μM), the PL maxima of **PCS1** was red shifted and increased at 515 nm as noticed in Figs. 7d, S14b, and S15b (ESI). But, after the addition of 0.5 equiv. (10 μM) of metal ions, the peak at 515 nm observed a slight quenching. Hence, the job's plots were plotted between X *vs* $(I-I_0)^*X$ for **PCS1**---M^{3+}, where it go through a maximum at molar segments of ca. 0.656 (**PCS1**---Fe^{3+}), 0.621 (**PCS1**---Cr^{3+}) and 0.628 (**PCS1**---Al^{3+}), respectively, as Shown in Figures 8b and S16 (ESI), representing the 2:1 stoichiometric complexes. In addition, the appearance of two isosbestic points at 320 and 375 nm in UV-Vis titrations of **PCS1**---

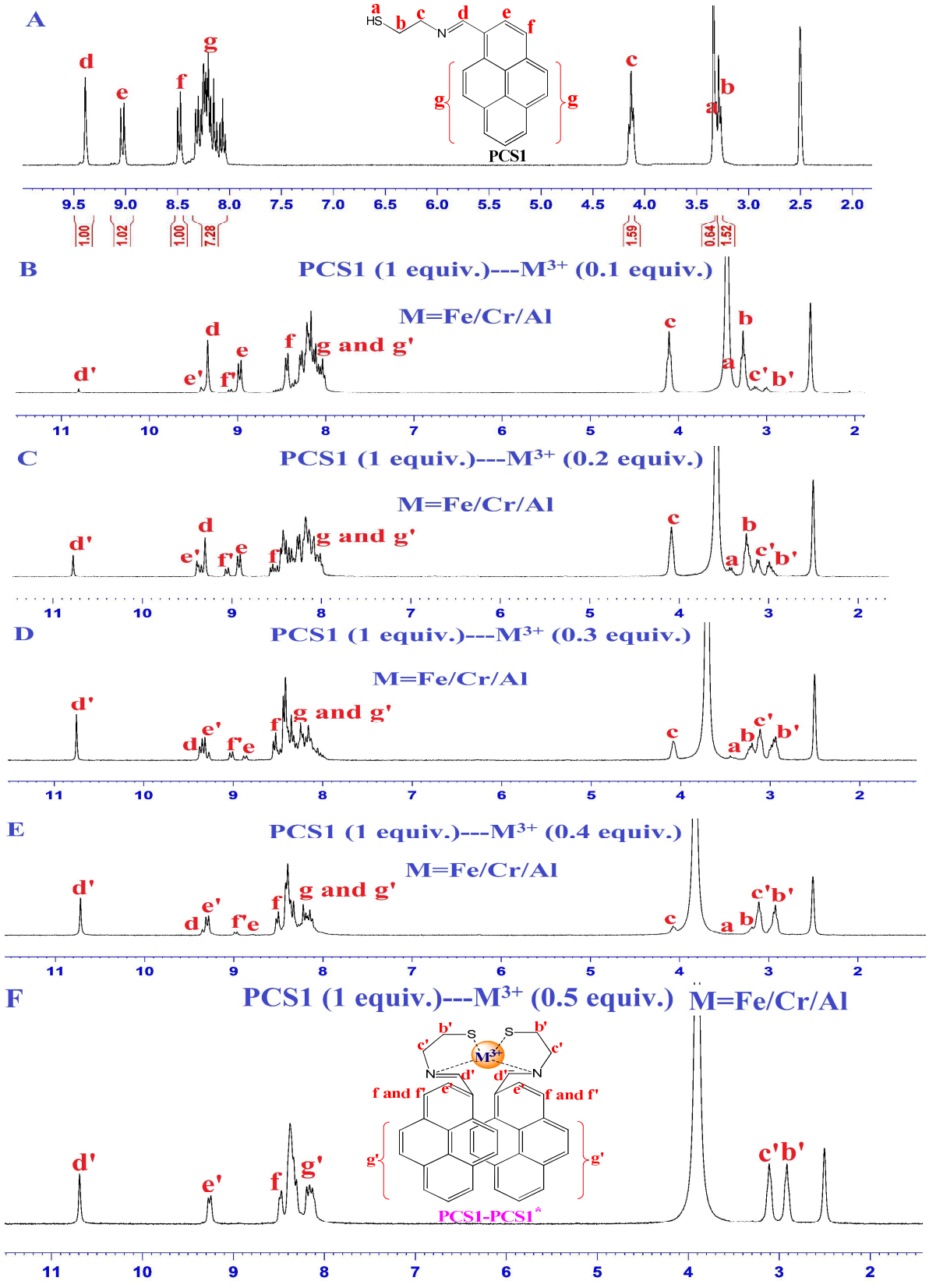

Fig. 9 (A-F) ^{1}H NMR spectral changes of **PCS1** (20 mM) in d6-DMSO with 0 - 10 mM (0.1 – 0.5 equiv.) of M^{3+} (M = Fe/ Cr/ Al) in D_2O.

M^{3+} [Figs. 7e, S14a and S15a (ESI)] also confirmed the definite possibility of 2:1 stoichiometry. Furthermore, the FTIR peaks of **PCS1**---M^{3+} by fixing M^{3+} ions as 1 equiv. with different **PCS1** variations (1 and 2 equiv.) also supported the 2:1 sensor complexes and excimer formations as remarked in Figure S17 (ESI). In which, the peak at 3387 cm^{-1} was corresponds to free –SH groups and the peak at 3240 cm^{-1} was related to hydrogen bonded –SH groups. The free –SH peak at 3387 cm^{-1} was disappeared at 1:1 complex of **PCS1**---M^{3+}. On the other hand, the hydrogen bonded –SH groups at 3240 cm^{-1} and the aliphatic $-CH_2$ stretching and vibrational peaks from 2850 to 3050 cm^{-1} were completely disappeared and broadened at 2:1 complex of **PCS1**---M^{3+}. Therefore, the 2:1 stoichiometry of **PCS1**---M^{3+} sensor complexes were well supported.

To verify the 2:1 stoichiometry of **PCS1**---M^{3+} sensor complexes, ESI (+Ve) mass spectral analysis of FTIR samples were performed. Delightfully, mass spectra of **PCS1**---M^{3+} complexes were confirmed their 2:1 stoichiometry by their assigned peaks as demonstrated by Figs. S18-S20 (ESI). Aimed at **PCS1**---Fe^{3+} and **PCS1**---Cr^{3+} complexes the ESI(+Ve) peaks were obtained at m/z = 630.4 $[(\mathbf{PCS1})_2\text{---}Fe^{3+}\text{- }2]^+$ and m/z = 629.4 $[(\mathbf{PCS1})_2\text{---}Cr^{3+}\text{+1}]^+$, respectively (Figures S18 and S19). Similar to them, **PCS1**---Al^{3+} complex ESI (+Ve) mass peak was found at m/z = 604.4 $[(\mathbf{PCS1})_2\text{---}Al^{3+}\text{ +1}]^+$ as exposed in Figure S20. Henceforth, formation of 2:1 stoichiometric **PCS1**---M^{3+} complexes were well approved. Additionally, the **PCS1**---M^{3+} (M = Fe/ Cr/ Al) sensor complexes were found to be reversible to their original state, during the addition of 10 μM of pent methyl diethylene diamine (PMDTA)[50, 52] in CH_3CN and can be reusable up to 4 cycles as demonstrated in Figs. S21-S23 (ESI). Therefore, the possible PET based sensing mechanism based on the excimer formation was proposed based on stoichiometry, FTIR and ESI (+Ve) mass studies as noted in Figure S24. By assuming a 2:1 complex formation, the association constants (K_a) of **PCS1**---M^{3+} were calculated on the basis of the following equation (1).[66]

$$\alpha^2/(1-\alpha) = 1/2K_aC_F\,[M] \quad \text{---------- (1)}$$

Where C_F is the total concentration of probe **PCS1** in the system and α is defined as the ratio between the free probe **PCS1** and the total concentration of probe **PCS1**. The value "α" was obtained using Eq. (2)

$$\alpha = F\text{-}F_0/F_1\text{-}F_0 \quad \text{---------- (2)}$$

F is the fluorescence intensity at 515 nm at any given M^{3+} (M = Fe/ Cr/ Al) concentration, F_1 is the fluorescence intensity at 515 nm in the absence of M^{3+} ions, F_0 is the maxima fluorescence intensity at 515 nm in the presence of M^{3+}. The association constants K_as were estimated graphically by plotting $\alpha^2/(1-\alpha)$ against $1/[M^{3+}]$. The plots $\alpha^2/(1-\alpha)$ vs. $1/[M^{3+}]$ are shown in Figs. S25 a-c (ESI). Data were linearly fitted with respect to Eq. (1) and the K_a values were obtained from their slopes. The K_a values of **PCS1**---M^{3+} (M = Fe/ Cr/ Al) were estimated as 2.25 x 10^6 M^{-2}, 2.13 x 10^6 M^{-2} and 2.02 x 10^6 M^{-2}, respectively. Further, to prove the selectivity of **PCS1** towards M^{3+} ions, the detection limits (LODs)[67] calculations were performed by standard deviation and linear fittings [Figs. 8c and S26 (ESI)]. By plotting the relative fluorescence intensity (I/I_0) changes as a function of concentration of M^{3+} ions, the detection limits of **PCS1**---M^{3+} complexes were estimated as 9.834 x 10^{-7} M (**PCS1**---Fe^{3+}), 9.9231 x 10^{-7} M (**PCS1**---Cr^{3+}) and 2.434 x 10^{-6} M (**PCS1**--- Al^{3+}), correspondingly.

Next, the TEM images of **PCS1**---M^{3+} (Figs. S27a-d) were investigated to clarify their morphological changes. Contrast to non-aggregated and aggregated (in AIEEs) **PCS1**, moderate aggregation were visualized in **PCS1**---M^{3+} sensor complexes (Note: The TEM studies were performed after 100 times dilution of samples). Hence, confirmed the nanocrystalline changes in excimer assisted **PCS1**---M^{3+} sensor complexes. Further, we performed pH titration of **PCS1** to investigate a suitable pH ranges for M^{3+} ions detection. Delightfully, during this analysis (pHs 1-14); the green "OFF-ON" emission enhancement were observed between pHs 1-3. On the other hand, higher pHs (11-14) are favorable for dimeric unit (**PCS2**) formation as stated in synthesis part. Therefore, as shown in Fig. S28 (ESI), the **PCS1**---M^{3+} sensors selectivity were verified between 4-10 pHs, maintained by the respective buffers (100 μM). The separate titrations of **PCS1** between pHs 5-10, not showed any fluorescence enhancement at 515 nm. Similarly, the **PCS1**---M^{3+} sensor complexes were not affected at pHs 6 and 7. Therefore, performing sensor titrations in CH_3CN solvent medium by maintaining the pH as 6 or 7 is highly appreciated.

Following, TRPL studies were taken into consideration to establish their PL life time (decay constant) changes during the sensor complexes (**PCS1**---M^{3+}) formation. As shown in Figs. 8d and S29 (ESI), the TRPL spectrum of **PCS1** was affected extremely in **PCS1**---M^{3+} complexes. Tables 1 and S1, summarized the respective comparable TRPL changes. Initially, the average TRPL decay constant (τ_{Avg}) of **PCS1** (in CH_3CN) was found as 3.105 ns. But, during **PCS1**---M^{3+} complexes formation, the decay constant increased to 5.94, 4.96, and 4.66 ns for **PCS1**---Fe^{3+}, **PCS1**---Cr^{3+}, and **PCS1**---Al^{3+}, respectively. Likewise, the faster and longer decay components (A_1 and A_2) were also affected along with their ultra-fast and longer decay constant (τ_1 and τ_2) values as summarized in Table S1.

To ensure the binding site and stoichiometry, the ^1H NMR titrations[68] were done as presented in Figs. 9A-F. For better understanding of peak shifts in the ^1H NMR of **PCS1**, the peaks were assigned as **a-g** and **a, b'-g'** for free and complexed states, correspondingly. Upon the addition of 0-0.5 equiv. of M^{3+} ions (with an equal span of 0.1 equiv.) in D_2O to **PCS1** in d_6-DMSO, the –SH (**a**) peak at 3.353 ppm (mixed with solvent peak) was initially upfield shifted to 3.251 up to 0.3 equiv., then completely disappeared at 0.4 equiv. of metal ions. Hence, confirmed the involvement of free –SH group in the complex formation. Similarly, the initial aliphatic peaks ($-CH_2\text{-}CH_2$; **b** and **c** in **PCS1**) observed at 3.27 and 4.11 ppm were slowly disappeared along with the upfield shifted newer peaks (**b'** and **c'** in **PCS1**---M^{3+}) at 2.92 and 3.11 ppm, respectively, which confirmed the possible binding of both hetero atoms (S and N) and their chelation to form the excimer **PCS1**-**PCS1*** for the sensing mechanism. The involvement of hetero atom (N) was well demonstrated by the observed changes for peak –CH=N (**d** in **PCS1**) as noted below. During **PCS1**---M^{3+} complex formation, the –CH peak of –CH=N was slowly vanished at 9.39 ppm and downfield shifted to 10.74 ppm (**d'**). Therefore, it is well

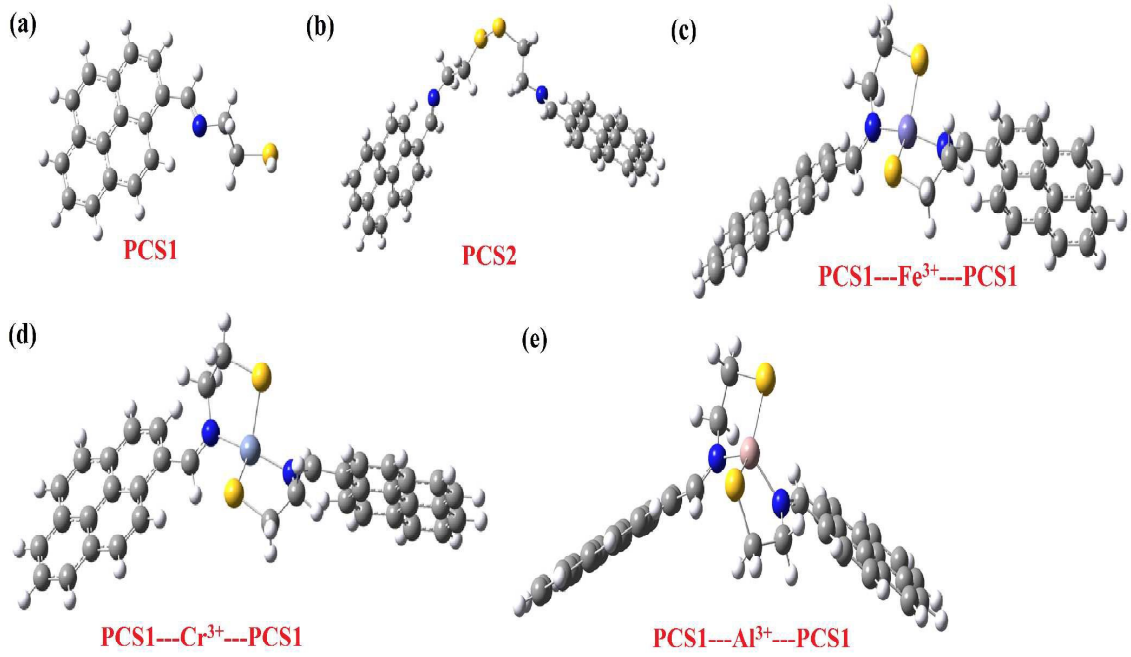

Fig. 10 Optimized structure of (a) **PCS1** (b) **PCS2** (c-e) **PCS1---**M^{3+} (M = Fe/ Cr/ Al) complexes at B3LYP/LANL2DZ level in gas phase. Grey-Carbon; White-Hydrogen; Yellow-Sulfur; Blue-Nitrogen; Gentian-Iron; Light blue-Chromium; baby pink-Aluminium.

verified the involvement of both –SH and N atom (in –CH = N) for the complex formation. Further, related results were obtained for aromatic **e-g** peaks of **PCS1** as described continuously. Due to the formation of metal induced **PCS1**-**PCS1*** excimer formation, the peak **e** (in **PCS1**) also slowly absent at 9.01 with downfield shifted peak appearance at 9.38 ppm. On the other hand, the other aromatic peaks **f** and **g** were also down field shifted (**f'** and **g'**) up to 0.3 equiv., i.e: during the co-ordination of **PCS1** to M^{3+} ions. Thereafter, they are found to be restored to their original state with broadened spectra from 0.4 - 0.5 equiv. of metal ions. Supplementary, we also confirmed that the peak at 10.74 ppm is not the peak of pyrene-1-carboxaldehyde. Henceforward, along with the supports of FTIR and ESI (+Ve) mass, the ^{1}H NMR titrations well established the binding sites as well as the stoichiometry for **PCS1**---M^{3+} sensors and proved the excimer formation as noted in Fig. S24 (ESI).

DFT Studies

To further elucidate the experimental observation of PET based mechanism of **PCS1** and **PCS1**---M^{3+} (M = Fe/ Cr/ Al) complexes the quantum chemical calculations have been carried out based on density functional theory (DFT) using a Gaussian 09 program.[69] The ground-state structures of **PCS1** and **PCS1**---M^{3+} (M= Fe/ Cr/ Al) complexes were optimized with the hybrid generalized gradient approximation (HGGA) B3LYP[70] method in the gas phase. The probe **PCS1** and sensor complexes **PCS1**---M^{3+}, were optimized by using the B3LYP method and its structures with electrostatic potential surface (ESP) were depicted in Fig. 1a. Electrostatic potential of **PCS1 (**see Figure 1a), has revealed the binding location of metal atoms which is shown in red colour. The schematic representation of optimized structures of **PCS1**---M^{3+} complexes and the distance between metal and N, S are shown in Fig. S32 (ESI). As shown in Fig. S32 (ESI), the distance between the M^{3+} (M = Fe/ Cr/ Al) and two S atoms of **PCS1** has been observed to be ~2.236 - 2.84295 Å. Similarly, the distance between M^{3+} and two N atoms have fallen between ~1.971 to 2.044 Å. The HOMO, LUMO and HOMO-LUMO gaps (HLGs) have been reported in Table 1. The frontier molecular orbital diagrams of HOMO and LUMO have also been generated at B3LYP/gen level and the respective electron localization structures are shown in Figs. S30 and S33 – S35 (ESI). The band gap between HOMO (-5.60 eV) and LUMO (-2.23 eV) of **PCS1** was calculated as 3.37 eV. On the other hand, due to the formation of excimer (**PCS1**-**PCS1***) *via* **PCS1**---M^{3+} coordination, the band gaps between the HOMOs (-8.02 eV, -8.02 eV and 8.26 eV) and LUMOs (-5.55 eV, 5.46 eV and 5.39 eV) of **PCS1**---Fe^{3+}, **PCS1**---Cr^{3+} and **PCS1**---Al^{3+} complexes have decreased to 2.47 eV, 2.56 eV and 2.87 eV, respectively, as compared to **PCS1**. Further, the initial electron transfer from HOMO to HOMO-1 may restrict the electron transfer process from HOMO-1 to LUMO. So, the PET process in **PCS1** has supressed the emission property. However, upon chelation to M^{3+} ions, the formation of excimer (**PCS1**-**PCS1***) evidenced the electron densities were located differently on **PCS1**---M^{3+} (M= Fe/ Cr/ Al) complexes compared to **PCS1** as shown in Figs. S30 and S33 – S35 (ESI). In **PCS1**---M^{3+} sensor complexes, the HOMO-1 electron densities were mainly located towards the metal ions. Whereas, the electronic clouds of HOMOs and LUMOs were localized on the different pyrene rings. Therefore, the electron transfer from HOMO-1 to HOMO in **PCS1---**M^{3+} complexes were inhibited and enhanced the electron transfer from HOMO to LUMO. During this

process, the PET of **PCS1** was supressed to provide the emission intensity with M^{3+} ions. The DFT based explanations have also been confirmed the 2:1 ratio of excimer sensor complexes formations and PET based fluorescent turn-on sensor responses of **PCS1** for M^{3+} ions detection. Fig. 10, illustrates the optimized structures of **PCS1**, **PCS2**, and **PCS1**---M^{3+} complexes. Based on the above explanations the proposed PET based general mechanistic representation for **PCS1**---M^{3+} sensor complexes has been shown in Fig. 11. As noticed in Figure S32, the **PCS2** also evidenced the PET mechanism in its original state. But, due to the intramolecular distance induced by –S-S- bond and the absence of free thiol group, **PCS2** does not show any selectivity to M^{3+} ions *via* excimer formation.

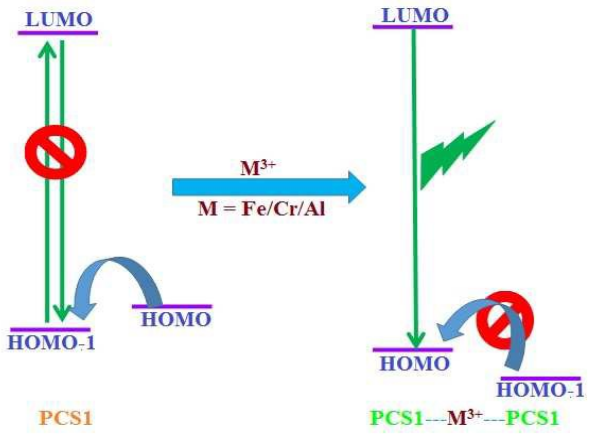

Fig. 11 General representation of PET based mechanism for **PCS1**---M^{3+} (M = Fe/ Cr/ Al) sensor system.

Living cell imaging

The potential of **PCS1** for imaging of M^{3+} (M = Fe/ Cr/ Al) in living cells were obtained using a confocal fluorescence microscope. When Raw264.7 cells were incubated with **PCS1** (20 µM), no fluorescence was observed (Fig. 12). After the treatment with M^{3+}, a bright green fluorescent images were observed in the Raw264.7 cells (Figure 12). An overlay of fluorescence and bright-field images shows that the fluorescence signals are localized in the intracellular area, indicating a subcellular distribution of M^{3+} ions and good cell-membrane permeability of **PCS1**.

Highly acidic pH sensing[71]

As discovered in the effect of pH on **PCS1**---M^{3+} sensor system, we have observed the 'OFF-ON" turn-on response of **PCS1** for highly acidic pHs (1-3). Hence, we tend to analysis in that direction with great attention by using both monomer/ dimer (**PCS1** and **PCS2**) compounds. Upon the addition of 1 M buffers 1-14 (50 µL) to 950 µL of **PCS1** / **PCS2** (20 µM in CH_3CN / DMSO), both evidenced the "OFF-ON" green fluorescent response at 505 nm (λ_{ex} = 410 nm) for highly acidic pHs 1-3 as shown Figs. S36a and S37a. In which, **PCS1** shown 256, 197, and 138 folds of PL with 71, 52, and 36 folds *of* Φ_f values enhancements to pHs 1-3, respectively. Similarly, **PCS2** also displayed the 87, 61, and 44 folds of PL with 31, 23, and 14 folds of Φ_f values enhancements towards pHs 1-3, in turn. The FTIR spectral peaks (not shown) of **PCS1** and **PCS2** evidenced the similar spectrum and also confirmed the presence of free thiol (-SH) unit with broadened peak at 3260 cm^{-1}. Further, formation of **PCS1** from **PCS2** in 1 M HCl was well confirmed by the ESI (+Ve) mass spectra (Fig. S8; ESI). To well establish the fluorescent signals were not from the imine hydrolysis, we performed the ^{1}H-NMR titrations (not shown) with 1M HCl in D_2O. Both compounds evidenced the similar broadened spectrum of **PCS1** confirmed the imine stability at higher acidic pHs (1-3) as supported by the mass spectra. On the other hand, the ^{1}H-NMR spectra of pyrene-1-carboxaldehyde at pH = 3.0 was completely differs from the **PCS1** with blue emission rather than green emission. Therefore, the green emission may arose from the possible self-aggregation / self excimer formation of **PCS1**. Hence, the possible self-aggregation / self excimer formation during pHs 1-3 was proposed in Fig. S38 (ESI). The real time *in-vitro* live cell applications was performed with pH = 3.0 buffer as stated before. RAW264.7 cells cultured in DMEM were treated with of 20 µM **PCS1** or **PCS2** dissolved in DMSO-sterilized pH = 3.0 buffer and incubate for 50 min., at 37°C. After the treatment with pH = 3.0 buffer, a bright / dismal green fluorescent images were observed in the Raw264.7 cells (Fig. S39; ESI). An overlay of fluorescence and bright-field images shows that the fluorescence signals are localized in the intracellular area, indicating a subcellular distribution of pH = 3.0 buffer and good cell-membrane permeabilities of **PCS1** and **PCS2**.

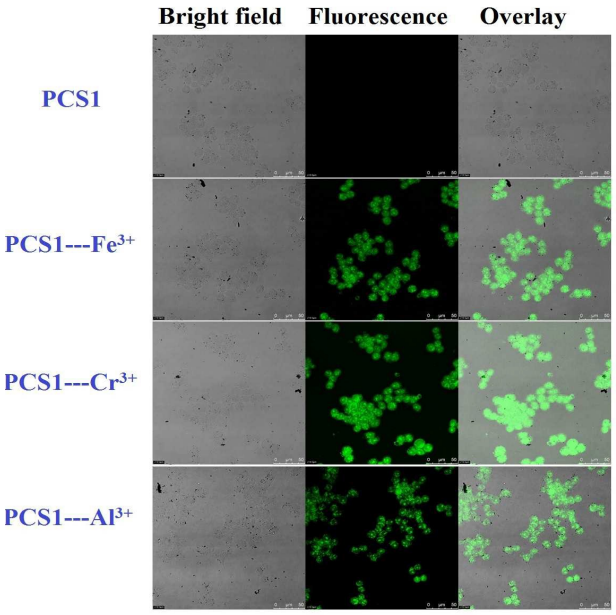

Fig. 12 Fluorescence images of Raw264.7 cells treated with **PCS1** and **PCS1**---M^{3+} (M = Fe/ Cr/ Al). Bright Field image (Left); Fluorescence image (middle); Merged image (right). The scale bar is 50 µM.

Additionally, the TEM images (Fig. S40; ESI) of **PCS1** and **PCS2** at pH = 3 buffer also demonstrated the differential nano-crystalline

Table 1 DFT results and photophysical properties for sensory and AIE studies of **PCS1** and **PCS2**.

Composition	HOMO[a] (eV)	LUMO[a] (eV)	HLG[a] (eV)	λ_{abs}[b] (nm)	λ_{em}[c] (nm)	Φ_f[d]	τ (ns)[e]
PCS1 (0%)	-5.60	-2.23	3.37	356	421	0.011	3.105
PCS1---Fe^{3+}	-8.02	-5.55	2.47	445	515	0.601	5.74
PCS1---Cr^{3+}	-8.02	-5.46	2.56	445	515	0.594	4.96
PCS1---Al^{3+}	-8.26	-5.39	2.87	445	515	0.207	4.66
PCS1 (80%)	ND	ND	ND	364, 393	465	0.5526	4.813
PCS2 (0%)	-5.58	-2.25	3.33	352	425	0.0152	1.345
PCS2 (60%)	ND	ND	ND	357, 396	469	0.854	1.856
PCS2+HCl	ND	ND	ND	443	505	0.218	0.72

[a]HOMO, LUMO, and HOMO-LUMO gaps are calculated with the B3LYP/gen method; [b]Experimental results of absorption band; [c]λ_{em}; Experimental results of emission band; [d]Quantum yields were calculated using Anthracene (Φ_f = 0.29 in ethanol) as a reference standard; [e] Obtained from time resolved fluorescence measurement; ND = not detected.

aggregation of them, contrary to **PCS1**---M^{3+} system. Hence, the possible PET supressed self-excimer formation (Figure S38, ESI) was appropriate. Furthermore, contrary to water soluble probes both **PCS1** and **PCS2** can be applied for device based sensory detection of those pHs in near future as mentioned earlier.

Conclusions

In conclusion, novel pyrene based monomeric and dimeric schiff base derivatives **PCS1 / PCS2** were synthesized via one-pot reaction with AIEEs characteristics. Their AIEEs and *J*-type nano-aggregation nature were well demonstrated by UV/PL, quantum yield (Φ_f) calculations, TEM, and DLS studies. Contrary to **PCS2**, only **PCS1** shows "OFF-ON" fluorescent selectivity to M^{3+} (M = Fe/ Cr/ Al) ions *via* excimer formation. The 2:1 stoichiometry of sensor complexes **PCS1---**M^{3+} (M = Fe/ Cr/ Al) were calculated and confirmed from job's plots based on PL titrations, FTIR and ESI (+Ve) mass analysis. In addition, the binding sites of sensor complex **PCS1---**M^{3+} were well established from ^{1}H NMR titrations. Hence, the possible PET based sensing mechanism through excimer (**PCS1**-**PCS1***) formation was proposed and supported through DFT calculations. By standard deviation and linear fittings the detection limits (LODs) were calculated as 10^{-7} M for Fe^{3+} and Cr^{3+} ions with discriminated detection of Al^{3+} ions at 10^{-6} M limit. The association constants (K_as) of **PCS1---**M^{3+} (M = Fe/ Cr/ Al) were estimated as 10^6 M^{-2} by standard deviation and linear fittings. Delightfully, both **PCS1** and **PCS2** evidenced the "OFF-ON" fluorescent turn-on response to pHs 1-3 and allow us to move in the direction of development of pH induced reaction based molecular switches. More importantly, AIEEs (**PCS1** and **PCS2**), sensor selectivity of **PCS1** to M^{3+} ions, and highly acidic pH sensors were successfully applied in cell imaging with cell viability analysis as well. Furthermore, development of device based sensors towards those identified analytes by the utilization of **PCS1** and **PCS2** are on the way.

Acknowledgements

The authors are grateful to the Ministry of Science and Technology of Taiwan for financially supporting this research under the contract MOST 103-2811-M-009-070 and MOST 102-2112-M-009-011-MY3.

Notes and references

1 (a) B. König, *Angew. Chem*., 1997, **36**, 530-531; (b) S. Muthaiah, M. V. Ramakrishnam Raju, A. Singh, H.-C. Lin, K.-H. Wei and H.-C. Lin, *J. Mater. Chem. A*, 2014, **2**, 17463-17476.
2 T. F. A. De Greef, M. M. J. Smulders, M. Wolffs, A. P. H. J. Schenning, R. P. Sijbesma and E. W. Meijer, Chem. Rev., 2009, **109**, 5687-5754.
3 M. Elhabiri and A.-M. Albrecht-Gary, *Coord. Chem. Rev*., 2008, **252**, 1079-1092.
4 (a) J.-M. Lehn, *Chem. Soc. Rev*., 2007, **36**, 151-160; (b) A. K. Dwivedi, M. Pandeeswar and T. Govindaraju, *ACS Appl. Mater. & Inter.*, 2014, **6**, 21369-21379.
5 (a) F. Würthner, T. E. Kaiser and C. R. Saha-Möller, *Angew. Chem*., 2011, **50**, 3376-3410; (b) S. Kamino, A. Muranaka, M. Murakami, A. Tatsumi, N. Nagaoka, Y. Shirasaki, K. Watanabe, K. Yoshida, J. Horigome, S. Komeda, M. Uchiyama and S. Enomoto, *Phys. Chem. Chem. Phys.*, 2013, **15**, 2131-2140.
6 D. M. Bassani, L. Jonusauskaite, A. Lavie-Cambot, N. D. McClenaghan, J.-L. Pozzo, D. Ray and G. Vives, *Coord. Chem. Rev*., 2010, **254**, 2429-2445.
7 (a) L. Wang, Y. Shen, Q. Zhu, W. Xu, M. Yang, H. Zhou, J. Wu and Y. Tian, *J. Phys. Chem. C*, 2014, **118**, 8531-8540; (b) S. Kamino, Y. Horio, S. Komeda, K. Minoura, H. Ichikawa, J. Horigome, A. Tatsumi, S. Kaji, T. Yamaguchi, Y. Usami, S. Hirota, S. Enomoto and Y. Fujita, *Chem. Comm.*, 2010, 46, 9013-9015.
8 M. Cai, Z. Gao, X. Zhou, X. Wang, S. Chen, Y. Zhao, Y. Qian, N. Shi, B. Mi, L. Xie and W. Huang, *Phys. Chem. Chem. Phys*., 2012, **14**, 5289-5296.
9 J. Gierschner, L. Lüer, B. Milián-Medina, D. Oelkrug and H.-J. Egelhaaf, *J. Phys. Chem. Lett*., 2013, **4**, 2686-2697.
10 (a) Y. Hong, S. Chen, C. W. T. Leung, J. W. Y. Lam, J. Liu, N.-W. Tseng, R. T. K. Kwok, Y. Yu, Z. Wang and B. Z. Tang, *ACS Appl. Mater. & Inter*., 2011, **3**, 3411-3418; (b) J.-H. Wang, H.-T. Feng and Y.-S. Zheng, *Chem. Comm.*, 2014, **50**, 11407-11410.
11 X. Wang, J. Hu, G. Zhang and S. Liu, *J. Am. Chem. Soc*., 2014, **136**, 9890-9893.
12 Y. Bao, H. De Keersmaecker, S. Corneillie, F. Yu, H. Mizuno, G. Zhang, J. Hofkens, B. Mendrek, A. Kowalczuk and M. Smet, *Chem. Mater*., 2015, **27**, 3450-3455.
13 L. Wang, Z. Zheng, Z. Yu, J. Zheng, M. Fang, J. Wu, Y. Tian and H. Zhou, *J. Mater. Chem. C*, 2013, **1**, 6952-6959.
14 A. Kathiravan, K. Sundaravel, M. Jaccob, G. Dhinagaran, A. Rameshkumar, D. Arul Ananth and T. Sivasudha, *J. Phys. Chem. B*, 2014, **118**, 13573-13581.
15 L. Wang, Y. Shen, M. Yang, X. Zhang, W. Xu, Q. Zhu, J. Wu, Y. Tian and H. Zhou, *Chem. Comm*., 2014, **50**, 8723-8726.
16 J. Wu, W. Liu, J. Ge, H. Zhang and P. Wang, *Chem. Soc. Rev*., 2011, **40**, 3483-3495.
17 (a) N. Niamnont, W. Siripornnoppakhun, P. Rashatasakhon and M. Sukwattanasinitt, *Org. Lett*., 2009, **11**, 2768-2771; (b) C. Han, T. Huang, Q. Liu, H. Xu, Y. Zhuang, J. Li, J. Hu, A. Wang and K. Xu, *J. Mater. Chem. C*, 2014, **2**, 9077-9082.
18 (a) N. Niamnont, R. Mungkarndee, I. Techakriengkrai, P. Rashatasakhon and M. Sukwattanasinitt, *Biosens. Bioelectron*., 2010, **26**, 863-867; (b) K. Y. Kim, S. H. Jung and J. H. Jung, *J. Mater. Chem. B*, 2015, **3**, 7222-7226.
19 (a) D. W. Domaille, E. L. Que and C. J. Chang, *Nat. Chem. Biol*., 2008, **4**, 168-175; (b) H.-T. Feng, S. Song, Y.-C. Chen, C.-H. Shen and Y.-S. Zheng, *J. Mater. Chem. C*, 2014, **2**, 2353-2359.
20 (a) S. Pal, N. Chatterjee and P. K. Bharadwaj, *RSC Adv*., 2014, **4**, 26585-26620; (b) S. H. Jung, K.-Y. Kwon and J. H. Jung, *Chem. Comm.*, 2015, **51**, 952-955; (c) H.-P. Fang, S. Muthaiah, A. Singh, M. V. R. Raju, Y.-H. Wu and H.-C. Lin, *Sens. Actuators B*, 2014, **194**, 229-237.
21 (a) D. Wencel, T. Abel and C. McDonagh, *Anal. Chem*., 2014, **86**, 15-29; (b) S. Muthaiah, Y. C. Rajan, P. Balu and A. Murugan, *New J. Chem.*, 2015, **39**, 2523-2531.
22 H. Zhu, J. Fan, B. Wang and X. Peng, *Chem. Soc. Rev*., 2015, **44**, 4337-4366.
23 B. Sui, S. Tang, T. Liu, B. Kim and K. D. Belfield, *ACS Appl. Mater. & Inter*., 2014, **6**, 18408-18412.
24 S. Samanta, S. Goswami, A. Ramesh and G. Das, *Sens. Actuators B*, 2014, **194**, 120-126.
25 S. K. Sahoo, D. Sharma, R. K. Bera, G. Crisponi and J. F. Callan, *Chem. Soc. Rev*., 2012, **41**, 7195-7227.
26 (a) Z. Chen, Y. Sun, L. Zhang, D. Sun, F. Liu, Q. Meng, R. Wang and D. Sun, *Chem. Comm*., 2013, **49**, 11557-11559.
27 O. V. Lushchak, O. I. Kubrak, O. V. Lozinsky, J. M. Storey, K. B. Storey and V. I. Lushchak, *Aquatic Toxicol*., 2009, **93**, 45-52.
28 V. Bencko, *J. Hyg., Epidemiol., Microbiol. Immunol*., 1985, **29**, 37-46.
29 (a) A. Levina and P. A. Lay, *Coord. Chem. Rev*., 2005, **249**, 281-298; (b) S. Muthaiah, T. Simon, K. W. Sun and F.-H. Ko, *Sens. Actuators B*, 2016, **226**, 44-51.
30 (a) S. Sivakumar, J. Sivasubramanian, C. Prasad khatiwada, J. Manivannan and B. Raja, *RSC Adv*., 2013, **3**, 20896-20904; (b) (b) D. Maity and T. Govindaraju, *Chem. Comm*., 2012, **48**, 1039-1041.
31 G. Berthon, *Coord. Chem. Rev*., 2002, **228**, 319-341.
32 S. Balasubramanian and V. Pugalenthi, *Talanta*, 1999, **50**, 457-467.
33 P. Lin and F. Yan, *Adv. Mater*., 2012, **24**, 34-51.
34 H.-J. Wang, X.-M. Du, M. Wang, T.-C. Wang, H. Ou-Yang, B. Wang, M.-T. Zhu, Y. Wang, G. Jia and W.-Y. Feng, *Talanta*, 2010, **81**, 1856-1860.
35 A. Barba-Bon, A. M. Costero, S. Gil, M. Parra, J. Soto, R. Martinez-Manez and F. Sancenon, *Chem. Comm*., 2012, **48**, 3000-3002.
36 D. Maity and T. Govindaraju, *Inorg. Chem*., 2010, 49, 7229-7231.
37 . Paul, A. Manna and S. Goswami, *Dalton Trans*., 2015, **44**, 11805-11810.
38 J. L. Pablos, P. Estevez, A. Munoz, S. Ibeas, F. Serna, F. C. Garcia and J. M. Garcia, *J. Mater. Chem. A*, 2015, **3**, 2833-2843.
39 Y. Urano, D. Asanuma, Y. Hama, Y. Koyama, T. Barrett, M. Kamiya, T. Nagano, T. Watanabe, A. Hasegawa, P. L. Choyke and H. Kobayashi, *Nat. Med*., 2009, **15**, 104-109.
40 M. Sauer, *Angew. Chem*., 2003, **42**, 1790-1793.
41 K. P. Carter, A. M. Young and A. E. Palmer, *Chem. Rev*., 2014, **114**, 4564-4601.
42 L. Zhu, K. Ploessl and H. F. Kung, Chem. Soc. Rev., 2014, **43**, 6683-6691.
43 S. Sarkar, S. Roy, A. Sikdar, R. N. Saha and S. S. Panja, *Analyst*, 2013, 138, 7119-7126.
44 (a) X. Sun, Y.-W. Wang and Y. Peng, *Org. Lett*., 2012, **14**, 3420-3423; (b) Y. Niko, S. Kawauchi, S. Otsu, K. Tokumaru and G.-i. Konishi, *J. Org. Chem.*, 2013, **78**, 3196-3207
45 (a) M. Kumar, A. Dhir, V. Bhalla, R. Sharma, R. K. Puri and R. K. Mahajan, *Analyst*, 2010, **135**, 1600-1605; (b) Y. Niko, Y. Cho, S. Kawauchi and G.-i. Konishi, *RSC Adv.*, 2014, **4**, 36480-36484.

46 B. Schazmann, N. Alhashimy and D. Diamond, *J. Am. Chem. Soc*., 2006, **128**, 8607-8614.
47 J. Mei, Y. Hong, J. W. Y. Lam, A. Qin, Y. Tang and B. Z. Tang, *Adv. Mater*., 2014, **26**, 5429-5479.
48 R. Chopra, P. Kaur and K. Singh, *Dalton Trans*., 2015, 2015, **44**, 16233-16237.
49 S. S. Babu, V. K. Praveen and A. Ajayaghosh, *Chem. Rev*., 2014, **114**, 1973-2129.
50 (a) S. Muthaiah, Y.-H. Wu, A. Singh, M. V. R. Raju and H.-C. Lin, *J. Mater. Chem. A*, 2013, **1**, 1310-1318; (b) Y. Zhou, C.-Y. Zhu, X.-S. Gao, X.-Y. You and C. Yao, *Org. Lett*., 2010, **12**, 2566-2569.
51 A. Singh, R. Singh, S. Muthaiah, E. C. Prakash, H.-C. Chang, P. Raghunath, M.-C. Lin and H.-C. Lin, *Sens. Actuators B*, 2015, **207**, 338-345.
52 (a) S. Muthaiah, Y.-H. Wu and H.-C. Lin, *Analyst*, 2013, **138**, 2931-2942; (b) S. Muthaiah, Y. C. Rajan and H.-C. Lin, *J. Mater. Chem*., 2012, **22**, 8976-8987.
53 P. T. Chivers and R. T. Raines, *Biochemistry*, 1997, **36**, 15810-15816.
54 C.-G. Freiherr von Richthofen, A. Stammler, H. Bögge and T. Glaser, *J. Org. Chem*., 2012, **77**, 1435-1448.
55 H. Golchoubian and F. Hosseinpoor, *Catal. Comm*., 2007, **8**, 697-700.
56 A. V. Joshi, S. Bhusare, M. Baidossi, N. Qafisheh and Y. Sasson, *Tetrahed. Lett*., 2005, **46**, 3583-3585.
57 C. E. Hoyle, A. B. Lowe and C. N. Bowman, Chemical Society Reviews, 2010, **39**, 1355-1387.
58 E. Besson, A. Mehdi, C. Reye and R. J. P. Corriu, *J. Mater. Chem*., 2009, **19**, 4746-4752.
59 L. Qu and G. Shi, *Chem. Comm*., 2004, 2800-2801.
60 A. P. H. J. Schenning, J. v. Herrikhuyzen, P. Jonkheijm, Z. Chen, F. Würthner and E. W. Meijer, *J. Am. Chem. Soc*., 2002, **124**, 10252-10253.
61 L. Wang, W. Li, J. Lu, Y.-X. Zhao, G. Fan, J.-P. Zhang and H. Wang, *J. Phys. Chem. C*, 2013, **117**, 26811-26820.
62 W. Wang, A. Fu, J. Lan, G. Gao, J. You and L. Chen, *Chem. Eur. J*., 2010, **16**, 5129-5137.
63 S. Chen, Y. Hong, Y. Zeng, Q. Sun, Y. Liu, E. Zhao, G. Bai, J. Qu, J. Hao and B. Z. Tang, *Chem. Eur. J*., 2015, **21**, 4315-4320.
64 M. Ramesh, Y.-R. You, S. Muthaiah, M.-C. Wu, H.-C. Lin and C.-W. Chu, *Org. Electron.*, 2014, **15**, 582-589.
65 Y.-Q. Weng, F. Yue, Y.-R. Zhong and B.-H. Ye, *Inorg. Chem*., 2007, **46**, 7749-7755.
66 H.-F. Wang and S.-P. Wu, *Sens. Actuators B*, 2013, **181**, 743-748.
67 J. Li, Y. Wu, F. Song, G. Wei, Y. Cheng and C. Zhu, *J. Mater. Chem*., 2012, **22**, 478-482.
68 W. Zhou, Y. Li, Y. Li, H. Liu, S. Wang, C. Li, M. Yuan, X. Liu and D. Zhu, *Chem. Asian J*., 2006, **1**, 224-230.
69 A. D. Becke, Phys. Rev. A, 1988, **38**, 3098-3100.
70 C. Lee, W. Yang and R. G. Parr, *Phys. Rev. B*, 1988, **37**, 785-789.
M. H. Lee, Z. Yang, C. W. Lim, Y. H. Lee, S. Dongbang, C. Kang and J. S. Kim, *Chem. Rev*., 2013, **113**, 5071-5109.

Table of Contents (TOC)

Novel pyrene based derivatives **PCS1 / PCS2** with AIEEs were reported as trivalent and pHs 1-3 sensors with live cell imaging.